



AUDITOR – GA 687367

Advanced Multi-Constellation EGNSS Augmentation and Monitoring Network and its Application in Precision Agriculture

D4.2 Version 2.0

Development and validation of sequential UBS and NABS models

Contractual Date of Delivery:	M16 (End of April, 2017)
Actual Date of Delivery:	09/05/2017
Editor:	Michael Schmidt (TUM);
Author(s):	Michael Schmidt, Eren Erdogan, Andreas Goss (TUM); Manuel Hernández-Pajares, Alberto García Rigo, Haixia Lyu (UPC);
Work package:	WP4 – Advanced Algorithms for GNSS
Security:	Public
Nature:	R
Version:	2.0
Total number of pages:	46

Abstract:

This document deals with the implementation of a sequential model for the vertical total electron content (VTEC) consisting of a global model part based on so-called uniform B-spline (UBS) functions and a regional model part for the area of investigation using so-called non-uniform adaptive B-spline (NABS) functions. Whereas the global part is estimated from near real-time GNSS observations, the regional densification part is determined from real-time high-resolution GPS data. The model result, i.e. the estimated VTEC can be projected into the direction of the ray path between the transmitting satellite and the receiver station by using the Barcelona Ionospheric Mapping (BIM) function in order to correct GNSS measurements, e.g., for precision agriculture.



Document Control

Version	Details of Change	Author	Approved	Date
1.0	Final complete version for EC review. Version numbering correction	MS, EE, AG, AGR, MHP, HL	MS, EE	05/05/2017
2.0	Final complete version for EC review	MS, EE, AG, AGR, MHP, HL	MS, EE, AGR	28/09/2017

Executive Summary

This document addresses the development of high-precision and high-resolution algorithms to provide enhanced models of the vertical total electron content (VTEC) within the Earth's ionosphere. This includes mainly two major points, namely (1) the improvement of existing mapping functions to convert the slant total electron content (STEC) measurable by GNSS into VTEC, and (2) the development of VTEC maps consisting of a global low-resolution model part and a regional high-resolution model part related to the area of investigation. The spectral content of the final VTEC product depends on the distribution of the input data, i.e. the GNSS observations.

To be more specific, the so-called Barcelona Ionospheric Mapping (BIM) function was derived at UPC from the TOMION model to fulfil the first issue mentioned above. For solving the second issue an enhanced VTEC model was developed by DGFI-TUM which is based on series expansions in terms of B-spline functions for both the global and the regional model parts. The corresponding series coefficients are estimated from globally distributed near real-time GNSS observations and from real-time GNSS observations available within the densification area, i.e. the area of investigation. The developed approach allows for the sequential processing of the observations. This document also contains intensive studies on the validation of the developed ionosphere model and dissemination strategies.

The document is divided in several sections. After introducing the problem in Section 1 the pre-processing of GNSS data is described in detail in Section 2. The Section 3 explains the data-adaptive VTEC representations already used at DGFI-TUM and further developed in WP 4 of the AUDITOR project for applications in precision agriculture. In Section 4 we describe in detail the different steps of the entire concept to provide high-resolution real-time VTEC maps. In Section 5 the VTEC representation in terms of so-called non-uniform adaptive B-splines (NABS) are compared with the corresponding expansions in terms of the uniform B-spline (UBS) functions. The Section 6 deals with the validation and verification of the ionospheric model results. The next Section 7 introduces the Barcelona Ionospheric Mapping (BIM) function. The deliverable ends with the conclusions in Section 8 and an extensive publication list in Section 9.

Authors

Partner	Name	e-mail
<u>DGFI-TUM</u>	Michael Schmidt	e-mail: mg.schmidt@tum.de
	Eren Erdogan	e-mail: eren.erdogan@tum.de
	Andreas Goss	e-mail: andreas.goss@tum.de
UPC	Manuel Hernández-Pajares	e-mail: manuel.hernandez@upc.edu
	Alberto García Rigo	e-mail: alberto.garcia.rigo@upc.edu
	Haixia Lyu	e-mail: haixia.lyu@upc.edu

Table of Contents

Document Control	2
Executive Summary	3
Authors	4
Table of Contents	5
List of Figures.....	6
List of Acronyms and Abbreviations.....	9
1. Introduction	11
2. Pre-processing of GNSS observations.....	15
Introduction	15
2.1 NRT GNSS data	15
2.2 RT GNSS data	16
2.3 Other space-geodetic observation techniques.....	16
2.4 Mapping Function	16
3. Data-adaptive VTEC representation	18
Introduction	18
3.1 1-dimensional modelling with Uniform B-Splines (UBS)	18
3.2 1-dimensional modelling with Non-Uniform Adaptive B-Splines (NABS).....	20
3.3 2-dimensional global modelling with UBS and NABS	21
3.4 2-dimensional regional modelling with UBS and NABS.....	23
3.5 Forecast model for the global UBS coefficients.....	24
3.6 Combination of global and regional VTEC representation	25
4. Concept of the high-resolution real-time VTEC model for selected densification areas	26
Introduction	26
4.1 Observation equations.....	26
4.2 Filter prediction model	27
4.3 Sequential Kalman Filtering	27
4.4 Overall modelling approach.....	28
5. Numerical investigations	30
Introduction	30
5.1 Global VTEC models based on UBS and NABS	30
5.2 Selection of global observation sites	31
5.3 Overall consistency of the global VTEC maps	32
5.4 Regional VTEC models based on UBS and NABS.....	33
5.5 Example of NABS solution in RT.....	35
6. Validation and verification of ionospheric model results.....	37
Introduction	37

6.1	Self-consistency analysis (dSTEC analysis)	37
6.2	Validation results	37
7.	Barcelona Ionospheric Mapping (BIM) function.....	40
	Introduction	40
7.1	Two-layer assumption.....	40
7.2	BIM modelling based on μ_2	40
7.3	Validation of the BIM-dSTEC assessment	41
8.	Conclusions	43
9.	References	44

List of Figures

Figure 1.1:	Layers of the atmosphere depending on the temperature (left) and on the degree of ionization (mid); vertical variation of the electron density within the ionosphere and the plasmasphere; orbit heights of selected satellites and satellite missions (right) (Limberger, 2015)	11
Figure 1.2:	Three often used parametrization methods in ionosphere modelling: spherical harmonics (left), grid-based voxel band above Earth (mid) and B-spline function representation (right). In the left and in the right case the horizontal model must be complemented by a vertical profiler for electron density modelling (Limberger, 2015).....	12
Figure 1.3:	The Single Layer Model (SLM) allow for the projection of STEC into VTEC by means of a mapping function depending on the elevation angle z . The projected VTEC value is spatially defined in the so-called ionospheric pierce point (IPP) which means the intersection of the ray path with the sphere of the SLM. The quantity H is called the effective ionospheric height (EIH).....	13
Figure 2.1:	Phase levelling along a continuous arc defined between a receiver and stellite pair in case of NRT data. The quantity $C = CPB_r^S$ as defined in Eq. (2.3) means the bias between the noisy code observations $P_{r,I}^S = P_4$ from Eq. (2.1) and the more precise but biased phase observations $L_{r,I}^S = L_4$ defined in Eq. (2.2).	15
Figure 2.2:	Locations of ionospheric observables from GPS, GLONASS, satellite altimetry, DORIS and IRO at February 11, 2016 at noon.	16
Figure 2.3:	Global distribution of efficient ionosphere height values (Hernández-Pajares et al., 2005).....	17
Figure 3.1:	Data-adaptive basis formations of the UBS (left panels) from different B-spline levels compared to the corresponding formations set up by the NABS (right panels). The red dots indicate the observation locations whereas the blue dots are the knots which are used to create the B-spline functions.	19
Figure 3.2:	Normalized endpoint-interpolating quadratic B-spline functions (3.2) for level $J = 3$. The set consists of $K_3 = 2^3 + 2 = 10$ B-spline functions. It can be seen from the red-	

- coloured curve that each B-spline is compactly supported, i.e. it is different from zero only a small part of the domain. Furthermore, it can be seen that the first two and the last two B-spline functions are modified by the endpoint-interpolating procedure; for more details see Schmidt (2007). 19
- Figure 3.3: Set of $K_2 = 3 \cdot 2^2 = 12$ trigonometric B-spline functions $T_{J,k}^2$ for $J = 2$. The red-coloured curve shows the the basis function $T_{2,2}^2$. The green-coloured curves mean the non-zero part of $T_{2,11}^2$ and show the "wrap-around" effect. 20
- Figure 3.4: IGS network with globally distributed stations with high coverage over Europe and huge data gaps over the oceans. However, meanwhile several islands are worldwide equipped with GNSS receiver stations. 22
- Figure 3.5: Distribution of the 2-D tensor products of normalized quadratic B-spline functions and trigonometric B-spline functions of the levels $J_1 = 3$ in latitude direction and $J_2 = 2$ in longitude direction. The tensor product of the two spline functions highlighted in black yields the shown 2-D function, as an example of a UBS function. Whereas in the 2-D representation light blue means a small positive value, the dark red colour represents the largest magnitude of up to value 1. 23
- Figure 3.6: Flowchart of the developed densification approach by combining a global B-spline model, estimated from global observations $L_{r,NRT}^S$, and a regional densification B-spline model computed from the regional observations $L_{r,RT}^S$ 25
- Figure 4.1: Overall flowchart of the developed NRT and RT modelling approach based on the B-spline representation 29
- Figure 5.1: Example for the distribution of knot points and basis functions in the NABS case (left panel) and the UBS case (right panel) with resolution levels $J_1 = 4$ along latitude and $J_2 = 3$ along longitude for hourly data at 12:00 UTC on April 2nd, 2017. The red line shows the prime meridian of Greenwich. 30
- Figure 5.2: NABS-based knot point distribution and basis function formation using the resolution levels $J_1 = 4$ for latitude and $J_2 = 3$ for longitude for hourly data at 12:00 UTC (left panel) and at 14:00 UTC (right panel) on April 2nd, 2017. The red line shows the prime meridian at Greenwich. The variations of the NABS with time are clearly visible, especially w.r.t. the longitude. 31
- Figure 5.3: NRT receiver station positions of the IGS network in red and the NRT EUREF network in blue (left panel); selected receiver stations after the data separation based on bin segmentation with a bin size of $10^\circ \times 10^\circ$ (right panel): the observations $L_{r,NRT}^S$, Eq. (2.4), from the selected receiver stations are used for global modelling according to Fig. 3.6. 32
- Figure 5.4: Examples of VTEC maps from IGS and its IAACs as well as the global solution of DGFI-TUM (top panel, mid column) at 12:00 UTC on March 3rd, 2017. 32
- Figure 5.5: Maps of the differences between the VTEC solutions from CODE, DGFI-TUM, JPL, UPC and ESA (from left to right and top to bottom) with respect to the IGS product at 12:00 UTC on March 3rd, 2017. 33
- Figure 5.6: Mean values and standard deviations of the VTEC differences with respect to the IGS product. 33

Figure 5.7: Examples of VTEC maps from CODE, DGFI's global NRT solution and the forecasted model solution based on Eq. (3.19) (first row from left to right) as well as the differences of DGFI's VTEC maps with respect to the CODE solution (second row). . 34

Figure 5.8: Regional distribution of NABS functions (left panel) for the RT input data (IPPs, blue dots) from the EUREF network and of UBS functions (right panel) with a regular knot distribution using the level values $J_1 = 3$ for latitude and $J_2 = 3$ for longitude at 12:00 UTC on April 2nd, 2017. The red line shows the prime meridian at Greenwich. 34

Figure 5.9: Overall procedure to compute the high-resolution regional VTEC maps in real-time. The exemplified follows the strategy introduced in the Figs. 3.6 and 4.1. 35

Figure 5.10: Exemplified VTEC solutions calculated according to the RT concept shown in Fig. 5.9 during ionospheric active times for Europe at 10:00 UTC (a), 12:00 UTC (b) and 14:00 UTC (c). The left column shows the VTEC maps derived from the forecast model using Eq. (3.19). The mid column represents the estimated $\Delta VTEC$ solutions according to Eq. (3.16) and the right column composes the total VTEC maps. 36

Figure 6.1: Analysis of the $dSTEC_{obs,k}$ values from a continuous arc by subtracting a reference observation. 37

Figure 6.2: European receiver stations used for the dSTEC analysis within the AUDITOR project. 38

Figure 6.3: Results of the statistical evaluation presenting the differences between the observed and the computed dSTEC values at the station 'YEBE' on April 2nd, 2017. 38

Figure 6.4: Results of the statistical evaluations presenting the differences between the observed and computed dSTEC values. 39

Figure 7.1: The diagram of BIM; IPP1 and IPP2 are the ionospheric pierce points along the ray path at the height values of the two layers. 41

Figure 7.2: IGS stations which are not used for the generation of the UQRG GIM in 2014 for external assessment of the BIM performance. The stations in blue were not used for statistical investigations due to very limited data for only a few available days. 42

List of Acronyms and Abbreviations

Term	Description
ARMA	Auto-Regressive and Moving Average
BKG	Federal Agency for Cartography and Geodesy, Bundesamt für Kartographie und Geodäsie
CODE	Center for Orbit Determination in Europe
CPB	Carrier Phase Bias
CPOB	Carrier Phase Observation Bias
DCB	Differential Code Bias
DGFI-TUM	German Geodetic Research Institute of the Technical University of Munich, Deutsches Geodätisches Forschungsinstitut der Technischen Universität München
DORIS	Doppler Orbitography and Radio Positioning Integrated by Satellite
DOY	Day of year
EIH	Effective ionospheric Height
EUREF	Regional Reference Frame Sub-Commission for Europe
ESA	European Space Agency
GEO	Geographic Coordinate System
GNSS	Global Navigation Satellite Systems
GLONASS	Russian Global Navigation Satellite System
GPS	Global Positioning System
GSM	Geocentric Solar Magnetic
IAAC	Ionosphere Associate Analysis Centres
IFB	Inter-Frequency Bias
IGS	International GNSS Service
IPP	Ionospheric Pierce Point
IRO	Ionospheric Radio Occultation
JPL	NASA Jet Propulsion Laboratory
IONEX	Ionosphere Map Exchange format
KF	Kalman Filtering
LOS	Line of Sight is the shortest distance between the satellite and the receiver.
NABS	Non-uniform Adaptive B-Splines
NRT	Near Real-Time

VTEC	Vertical Total Electron Content
RMS	Root Mean Square
RT	Real-Time
SCA	Self-Consistency Analysis
SH	Spherical Harmonics
SLM	Single Layer Model
STEC	Slant Total Electron Content
TECU	Total Electron Content Unit (1 TECU = 10^{16} electrons/m ²)
UBS	Uniform B-Splines
UPC	Universitat Politècnica de Catalunya

1. Introduction

As shown in Fig. 1.1, the Earth's atmosphere can be structured into various layers depending on different physical parameters. Following the temperature profile, for instance, the atmosphere can be split into troposphere, stratosphere, mesosphere, thermosphere, and exosphere. Following the degree of ionization, the atmosphere is composed of the neutral atmosphere up to approximately 50 km altitude, the ionosphere between 50 km and 1000 km, and the plasmasphere.

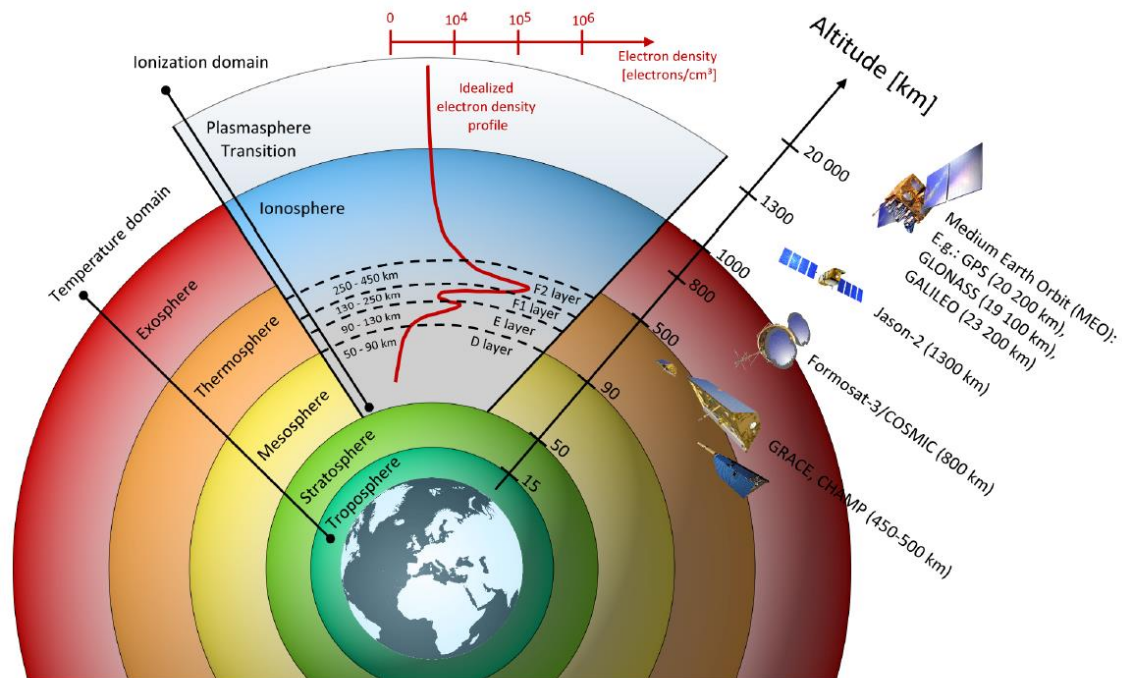


Figure 1.1: Layers of the atmosphere depending on the temperature (left) and on the degree of ionization (mid); vertical variation of the electron density within the ionosphere and the plasmasphere; orbit heights of selected satellites and satellite missions (right) (Limberger, 2015)

The knowledge of the structure and the dynamics of the ionospheric plasma has great importance for various applications, such as telecommunication through radio signals, point positioning or precision farming based on the Global Navigation Satellite Systems (GNSSs), e.g. GPS or GLONASS. Today, the advances in space-geodetic techniques, such as terrestrial GNSS, space borne radio occultation techniques as well as satellite altimetry, facilitates the monitoring of the structure of the ionosphere with an improved spatial and temporal resolution. Particularly, GNSS offers an attractive alternative to traditional methods, such as ionosondes, for monitoring the ionosphere. Consequently, in modern geodesy, the ionosphere is not only seen as a disturbing quantity which needs to be corrected, but also as a target quantity since almost all geodetic measurement techniques provide valuable information about the current state of the ionosphere.

The International GNSS Service (IGS) delivers large volumes of GNSS data with different latencies (e.g., real time, hourly) acquired from continuously operating terrestrial GNSS receivers distributed worldwide. The four IGS Ionosphere Associate Analysis Centers (IAACs), namely the Jet Propulsion Laboratory (JPL), the Center for Orbit Determination in Europe (CODE), the European Space Operations Center of the European Space Agency (ESOC) and the Universitat Politècnica de Catalunya (UPC), monitor the ionosphere and evaluate relevant parameters using dual frequency GNSS receivers.

GNSS observations

Two of the main error sources in precise positioning with GNSS are the ionospheric delay and the bending of the ray path of the electromagnetic signal. As GNSS signals propagate through the ionosphere they are affected by the free electrons excited from photo ionization through solar radiation.

As will be presented in Section 2.1 the basic near real-time (NRT) observable of GNSS for ionosphere modelling is the so-called phase-levelled geometry-free observation $\tilde{L}_{r,NRT}^s$ defined as

$$\tilde{L}_{r,NRT}^s = \alpha \cdot STEC + b_r + b^s + e_{L_{NRT}} \quad (1.1)$$

where the quantities b_r and b^s are the differential code biases (DCBs) of the receiver R and the satellite S , α is a frequency-dependent constant factor and $e_{L_{NRT}}$ accounts for the measurement error. The Slant Total Electron Content $STEC$ in Eq. (1.1) is according to

$$STEC = \int_s^r N_e dl \quad (1.2)$$

defined as the integration of the electron density N_e along the ray path between the transmitting satellite and the receiver. Inserting Eq. (1.2) into Eq. (1.1) yields the basic equation between high-precision GNSS phase observations and the electron density as the space- and time-dependent key quantity for ionosphere modelling. Due to physics-based thermosphere-ionosphere coupling processes the electron density plays also an important role in thermosphere modelling, e.g. relevant in satellite orbit determination, in particular for Low-Earth-Orbiting (LEO) satellites (Panzetta et al., in review) or space debris.

There are many approaches available for modelling the electron density N_e . Generally, these approaches can be categorized into the voxel-based approach and the function-based approach for ionosphere tomography (Liu et al., 2006). The voxel-based approach (see Fig. 1.2, mid part) assumes that the ionosphere can be subdivided into cells with constant electron density (see e.g., Hernández-Pajares et al., 1999; Juan et al., 1997; Kuklinski, 1997). The function-based one employs a set of basis functions modelling the vertical and horizontal variations of the ionosphere, respectively. For examples, Liu and Gao (2004) modelled the electron density correction term that is defined to be relative to an a priori electron density reference, horizontally by a series of spherical harmonic functions (see Fig. 1.2, left part) and vertically by Empirical Orthogonal Functions (EOF). Schmidt et al. (2008) represented the electron density correction term by a 2-D B-spline (longitude and latitude, see Fig. 1.2, right part)/1-D height-dependent EOF tensor product approach; see also Liu and Gao (2004) for the EOF analysis method. An approach of 3-D B-spline expansions with respect to longitude, latitude and height was also applied to model the electron density correction term (e.g., Schmidt, 2007; Zeilhofer et al., 2009). In addition, the height-dependency of the electron density is modelled by so-called ionosphere “profilers” (in the sense that they use “anchor points”, i.e., layer peaks and provide the vertical EDP between the anchor points, see Leitinger et al., 2001; Liang, 2017), such as the Chapman or the Epstein function.

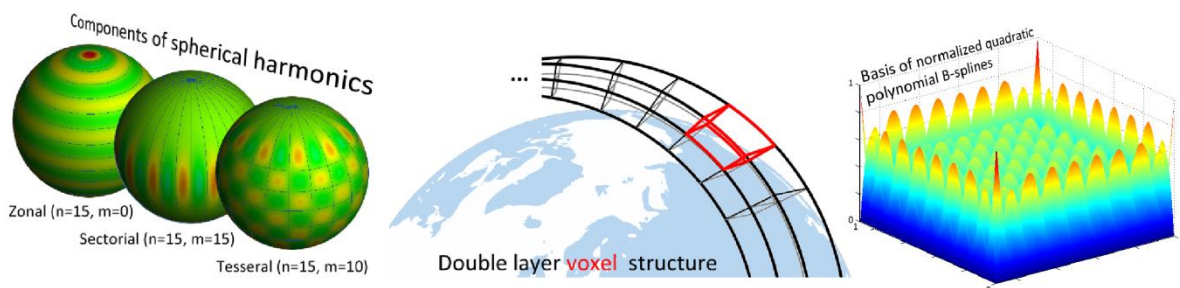


Figure 1.2: Three often used parametrization methods in ionosphere modelling: spherical harmonics (left), grid-based voxel band above Earth (mid) and B-spline function representation (right). In the left and in the right case the horizontal model must be complemented by a vertical profiler for electron density modelling (Limberger, 2015)

Generally, compared with the function-based approach, the voxel-based one is more flexible, as the spatial and temporal resolutions are not fixed within the region under investigation (Feltens et al.,

2011). However, the function-based approach allows the computation of the electron density everywhere within the region under investigation, whereas the voxel-based approach requires additionally interpolation (Liu et al., 2006). Besides a detailed overview about different representations Limberger (2015) emphasizes also their pros and cons. It is worth to be mentioned that the electron density depends not only on location but also on the solar cycle, the season and other parameters.

Mapping function

In case that the ray path is pointing into the vertical, STEC is denoted as the Vertical Total Electron Content (VTEC) defined as the integration of the electron density N_e along the vertical from the lower height h_b and the highest altitude h_t , i.e.

$$VTEC = \int_{h_b}^{h_t} N_e dh . \quad (1.3)$$

Mathematically, Eq. (1.3) transforms the 3-D electron density $N_e(\varphi, \lambda, h)$ depending on latitude φ , longitude λ and height h into the 2-D function $VTEC(\varphi, \lambda)$ defined on a sphere. Considering additionally the time dependency, Eq. (1.3) can be interpreted as the transformation of the 4-D function $N_e(\varphi, \lambda, h, t)$ into the 3-D VTEC value $VTEC(\varphi, \lambda, t)$. Besides the electron density, VTEC is the second key quantity of ionosphere modelling. Since the evaluation of the Eqs. (1.2) and (1.3) needs the application of numerical integration procedures, and GNSS measurements of higher elevation angles are not very sensitive with respect to height-dependent quantities, the integration along the ray path can be avoided by applying a simple mapping procedure as demonstrated in Fig. 1.3 and discussed in the following.

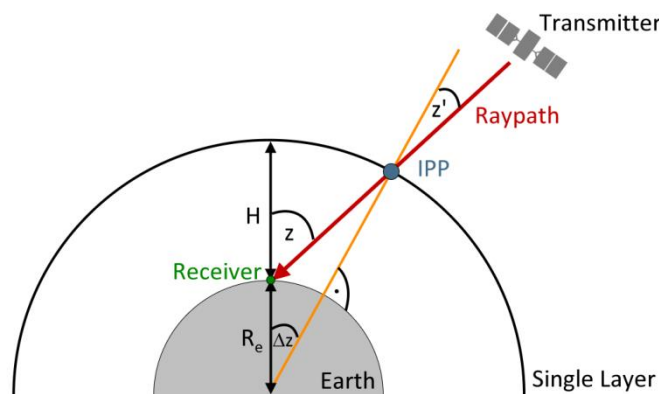


Figure 1.3: The Single Layer Model (SLM) allow for the projection of STEC into VTEC by means of a mapping function depending on the elevation angle z . The projected VTEC value is spatially defined in the so-called ionospheric pierce point (IPP) which means the intersection of the ray path with the sphere of the SLM. The quantity H is called the effective ionospheric height (EIH).

To be more specific, the SLM assumes that all free electrons of the ionosphere are concentrated in an infinitesimal thin shell above the Earth surface (Schaer, 1999) at an altitude H , i.e. the effective ionospheric height (EIH). Related to the SLM, a mapping function

$$m(z) = \frac{STEC}{VTEC} \quad (1.4)$$

is introduced as the ratio of STEC and VTEC. For instance, the Modified Single Layer Mapping Function (MSLM) developed years ago at CODE (Hugentobler et al., 2008; Dach et al., 2012) is widely accepted and for instance implemented in the Bernese software package 7 (Dach et al., 2007). It is defined as

$$m(z) = \frac{1}{\cos z'} = \left(1 - \left(\frac{R_e}{R_e + H} \sin(\alpha_m z) \right)^2 \right)^{-\frac{1}{2}} \quad (1.5)$$

with the numerical values $\alpha_m = 0.9782$ and $H = 506.7$ km are used. The mean Earth radius R_e is set to $R_e = 6371$ km.

The mapping (1.5) can be seen as a simple geometrical projection with an isotropic transformation function $m(z)$ just depending on the zenith angle z without any information about the horizontal structure of the ionosphere (Smith et al., 2008). Consequently, it can cause a serious degradation of the accuracy of the calculated VTEC values. This is the reason for various investigations on the EIH, which show that it varies with respect to the geographical location, the solar cycle, the time of the day, the elevation angle of the slant ray path, and the season (Brunini et al., 2011; Rama Rao et al., 2006; Birch et al., 2002; Komjathy and Langley, 1996) and the solar activity; for more details see also the Subsection 2.4 and the Section 7 of this report.

Global and regional VTEC modelling

In the context of Fig. 1.3 we introduced the IPP, which defines the spatial position $P_{IPP}(\varphi, \lambda)$ of the quantity $VTEC(\varphi, \lambda, t)$ related to a specific transmitter-receiver constellation. As already mentioned the IGS provides Global Ionosphere Maps (GIMs) with a latency of a few hours or even days or weeks. Each GIM is a combination of the individual solutions of the different IAACs and, thus, is only depending on the data of the global IGS network – with the exception of some additional receiver station, e.g. from the UNAVCO network. The GIMs represent the low-frequency part of VTEC – a spherical harmonic expansion up to degree and order 15 – and are therefore not convenient for regional applications such as precision agriculture. The reason for restricting the global model to the low-frequency part is the rather inhomogeneous distributed data over the globe including large data gaps, in particular, over the oceans, but also continental areas such as the Sahara Desert. To increase the spectral information of the model the resolution should be increased by adapting it to the data distribution.

For this purpose a densification procedure was developed within the AUDITOR project at DGFI-TUM which is based on B-spline expansions and allows for the combination of a low-resolution global and a high-resolution regional model part. Such a combined model consists of a global representation $VTEC_{glob}(\varphi, \lambda)$ for the low-frequency part and one or more regional densification parts $\Delta VTEC_{reg}(\varphi, \lambda)$ for the high-frequency variations according to

$$VTEC_{reg}(\varphi, \lambda) = VTEC_{glob}(\varphi, \lambda) + \Delta VTEC_{reg}(\varphi, \lambda). \quad (1.6)$$

It will be demonstrated in the following sections that the developed approach is solely based on B-spline expansions. The estimation of the target function $VTEC_{reg}(\varphi, \lambda)$ for the area under investigation, e.g. a densification area for precision agriculture and its error or standard deviation map in RT are the output quantities of the AUDITOR project part DGFI-TUM was working on.

Dissemination

Additionally, the project partner from UPC in Barcelona developed the so-called “Barcelona Ionosphere Mapping” (BIM) function which can be used to convert the estimated $VTEC_{reg}(\varphi, \lambda)$ values from Eq. (1.6) into the slant direction to get estimated STEC values valid for the area under investigation. This way, the estimated STEC value corrects the GNSS measurement which can be used, e.g., for precision farming. This procedure will be presented in detail in Section 7.

It was already stated in the deliverable D4.1 that there are basically two options for setting up a message based on B-spline modelling, namely providing

- (1) VTEC B-spline series coefficients (see the Eqs. (3.15), (3.16) and (3.19) for modelling the two parts on the right-hand side of Eq. (1.6)) or
- (2) VTEC grid values according to the left-hand side of Eq. (1.6).

In case of option (1) an encoder procedure for the coefficients is necessary, because the user has to evaluate the B-spline models just as in the SH case, only substituting the B-splines for the SHs. In the case of option (2) the regional VTEC grid values will be disseminated directly to the user. However, an additional interpolation procedure is necessary to compute a VTEC value at any arbitrary spatial location at any specific time.

2. Pre-processing of GNSS observations

Introduction

To extract ionospheric information from dual-frequency GNSS measurements, the geometry-free linear combination can be used (Ciraolo et al., 2007). Since we use both real-time and near real-time data we discuss both types of data processing and start in the following Subsection 2.1 with the latter one.

2.1 NRT GNSS data

From the GNSS dual-frequency code pseudo-range measurements P_{r,f_1}^S and P_{r,f_2}^S as well as the phase measurements Φ_{r,f_1}^S and Φ_{r,f_2}^S on the two carrier frequencies f_1 and f_2 between a satellite S and a receiver R the so-called geometry-free observations $P_{r,I}^S$ and $L_{r,I}^S$ for code and phase, respectively, are defined as

$$P_{r,I}^S = P_{r,f_2}^S - P_{r,f_1}^S = \alpha \cdot STEC + b_r + b^S - e_p, \quad (2.1)$$

$$L_{r,I}^S = \Phi_{r,f_1}^S - \Phi_{r,f_2}^S = \alpha \cdot STEC + B_r + B^S + C_{arc,r}^S - e_L. \quad (2.2)$$

In the Eqs. (2.1) and (2.2) the quantities b_r and b^S are the differential code biases (DCBs) of the receiver and the satellite, the abbreviations B_r and B^S stand for the receiver and the satellite inter-frequency biases (IFBs) and α is a frequency-dependent constant factor. Furthermore, $C_{arc,r}^S$ is the ambiguity bias of the carrier-phase, the quantities e_p and e_L account for the measurement errors.

The pseudo-range measurements are rather noisy but unambiguous, while the carrier-phase data are significantly more precise but biased. To exploit the precision of the phase measurements, an offset, the so called Carrier Phase Bias, CPB_r^S , including the parts IFB, DCB and $C_{arc,r}^S$, is computed by averaging the differences between $L_{r,I}^S$ and $P_{r,I}^S$ for every continuous arc that shares a common phase bias (Ciraolo et al., 2007, Mannucci et al., 1998) according to

$$CPB_r^S \approx \frac{1}{N} \sum_{j=1}^N (L_{r,I}^S - P_{r,I}^S)_j, \quad (2.3)$$

where N is the number of observations $j = 1, \dots, N$ measured along the arc. An elevation-dependent threshold is established to select the more precise observations with higher elevation angle for the computation of CPB_r^S . Then, a levelled geometry-free NRT phase observation $\tilde{L}_{r,NRT}^S$ for a continuous arc is defined as

$$\tilde{L}_{r,NRT}^S := L_{r,I}^S - CPB_r^S = \alpha \cdot STEC + b_r + b^S - e_{L_{NRT}}. \quad (2.4)$$

The levelling technique is applied to hourly data sets of GPS and GLONASS observations obtained from the IGS data servers.

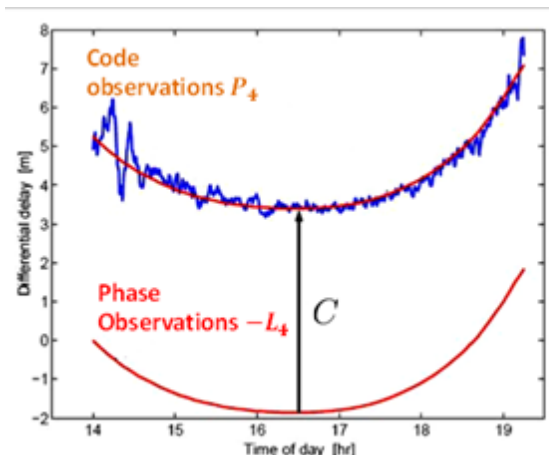


Figure 2.1: Phase levelling along a continuous arc defined between a receiver and satellite pair in case of NRT data. The quantity $C = CPB_r^S$ as defined in Eq. (2.3) means the bias between the noisy code observations $P_{r,I}^S = P_4$ from Eq. (2.1) and the more precise but biased phase observations $L_{r,I}^S = L_4$ defined in Eq. (2.2).

2.2 RT GNSS data

In the proposed RT modelling approach for the densification areas, we only utilize the GNSS phase measurements (2.2). In contrast to the levelled geometry-free NRT phase observations (2.4) where the relevant phase ambiguity biases are eliminated within the data pre-processing step, in the RT approach the phase related biases in Eq. (2.2) are directly estimated in the frame of Kalman filtering. After comprising the biases to one parameter, i.e. the Carrier Phase Observation Bias, $CPOB_r^s := B_r + B^s + C_{arc,r}^s$, the geometry-free phase observation equation used by the RT approach reads

$$\tilde{L}_{r,RT}^s := \alpha \cdot STEC + CPOB_r^s - e_{L_{RT}} \quad (2.5)$$

In our final approach the observation equations (2.4) and (2.5) are used both.

2.3 Other space-geodetic observation techniques

Additional techniques such as satellite altimetry, cf. the Jason-2/-3 missions, the Doppler Orbitography and Radiopositioning Integrated by Satellite (DORIS) system and Ionospheric Radio Occultations (IRO) from the Formosat-3/COSMIC mission have been analysed for suitability, i.e. for integration into the modelling procedure. As can be seen from Fig. 2.2 the additional observations reduce partly the inhomogeneity of the data distribution. However, due to very high latencies which can reach up to days these three observation techniques have not been used within the modelling process in AUDITOR since we intend NRT and RT processing.

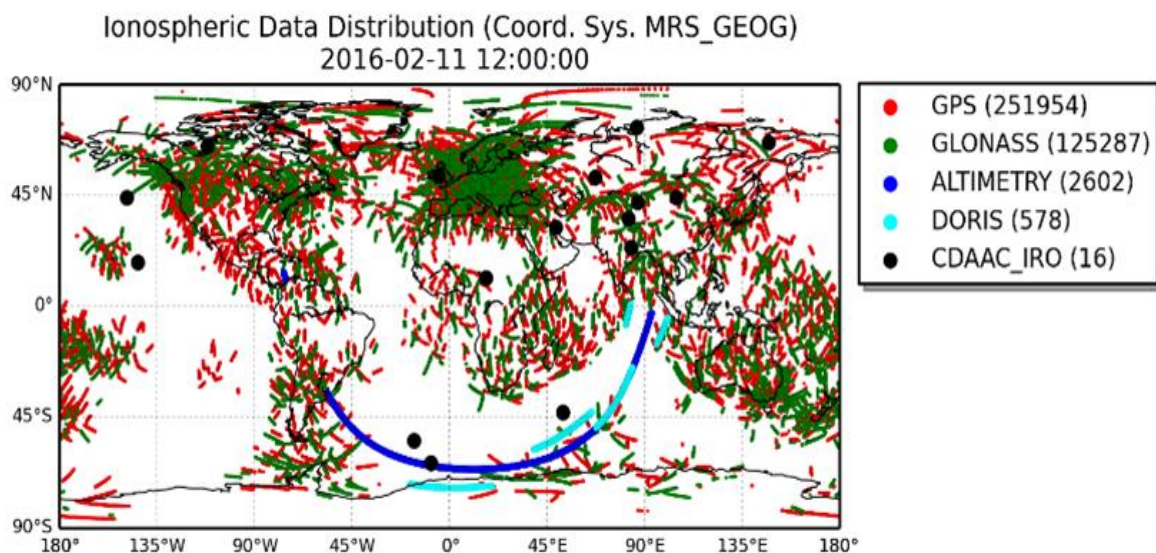


Figure 2.2: Locations of ionospheric observables from GPS, GLONASS, satellite altimetry, DORIS and IRO at February 11, 2016 at noon.

2.4 Mapping Function

As described before the height of the SLM, cf. Fig. 1.3, is typically set to a fixed value – mostly between 350 and 450 km. In our approach we chose instead the value 506.7 km as recommended by Dach et al. (2007) and already mentioned in the context of Eq. (1.5). As explained in the context of the Eq. (1.4) this value provides a more realistic approximation of the 2-D VTEC representation (1.3) by applying the single layer simplification. However, it has to be stated that a realistic mapping function depends on the actual electron distribution which varies with local time, latitude, solar activity and many other parameters.

It has been demonstrated in several previous studies that a fixed single layer height may introduce significant modelling errors (Komjathy and Langley, 1996; Birch et al., 2002). The research group gAGE of UPC also showed in one of the group's previous studies that the effective height for the mapping

function can vary significantly in time and location (Hernández-Pajares et al., 2005). Figure 2.3 demonstrates a typical snapshot of the EIH distribution as provided by the aforementioned study.

In the light of the discussion in the previous paragraph, besides the traditional single layer approach with a fixed height, a varying effective height is included in the study in order to get more realistic mapping function values. Related effective height data are produced from the tomographic ionospheric model (TOMION) with global ground-based GPS data, which is routinely used by gAGE to provide VTEC maps to IGS and real-time applications; see e.g. Fig. 1.2, mid panel, for the layout of the two-layer tomography model.

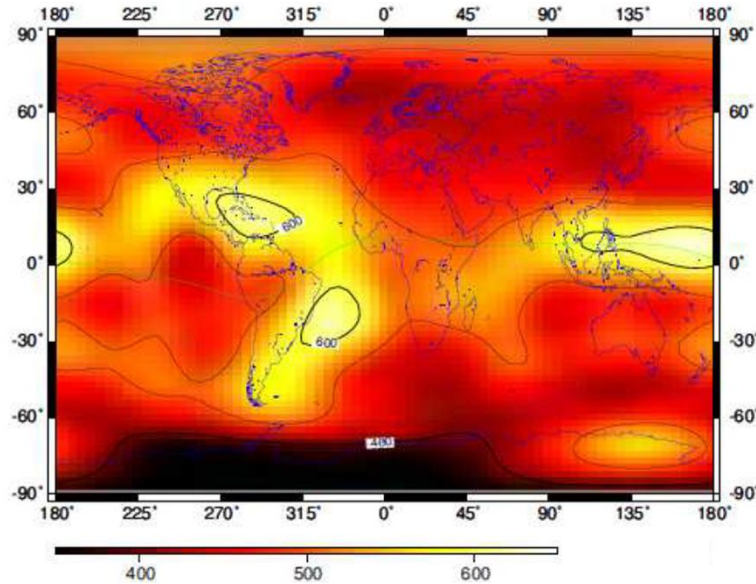


Figure 2.3: Global distribution of efficient ionosphere height values (Hernández-Pajares et al., 2005)

In the AUDITOR project a procedure was developed which uses two different mapping procedures. To be more specific, the following strategy was applied:

1. In the observation equations (2.4) and (2.5) we replace the quantity $STEC$ by the equation

$$STEC = m(z) \cdot VTEC \quad (2.6)$$

and use the mapping function (1.5) with the constant value $H = 506.7$ km for the EIH.

2. For the dissemination of our estimated VTEC model to the user in precision agriculture the Barcelona Ionospheric Mapping (BIM) function is applied. To be more specific, the application of the BIM function according to Eq. (7.3) for the computation of $STEC$ must be performed by the receiver software.

We justify this procedure by the fact, that for the setup of the observation equations (2.4) and (2.5) in NRT or RT, a high-resolution VTEC map for the area of investigation is not available. Thus the application of the BIM approach according to Eq. (7.3) can only be performed approximately. For that reason we use the traditional mapping function (1.5) which also means an approximation with a comparable accuracy. Since our computations have to be done in RT we prefer the more effective method (1.5) with a shorter computation time. For the dissemination the situation is totally different, since at that stage the high-resolution VTEC model according to Eq. (1.6) is available.

3. Data-adaptive VTEC representation

Introduction

The data-adaptive VTEC approach, based on B-Spline modelling, to be developed within the AUDITOR project by DGFI-TUM, means an adaptive technique to resolve the problem of the inhomogeneous data distribution (see Fig. 2.2). For this purpose a densification approach was developed which allows for the combination of a low-resolution global and a high-resolution regional model part. In this manner, the focus of the derivations in the following subsections is on the adaptive algorithms exploiting the advantages of B-splines for VTEC representation

To explain the B-spline approach in some detail we start with a 1-D representation in Subsection 3.1 although the VTEC model requires at least a 2-D approach. Consequently, we generalize the results from the 1-D case later to the 2-D case.

3.1 1-dimensional modelling with Uniform B-Splines (UBS)

Assuming a signal $f(x)$ given for $x \in \mathbb{R}$ (\mathbb{R} means the set of real numbers along the x -axis) can be represented by the series expansion

$$f(x) = \sum_{k=0}^{K_J-1} d_{J,k} N_{J,k}^2(x) \quad (3.1)$$

in terms of the normalized quadratic B-spline functions $N_{J,k}^2(x)$ of resolution level $J \in \mathbb{N}_0$ (\mathbb{N}_0 means the set of natural numbers including the "0") and shift $k = 0, 1, \dots, K_J - 1$ calculable recursively via the relation

$$N_{J,k}^m(x) = \frac{x - t_k^J}{t_{k+m}^J - t_k^J} N_{J,k}^{m-1}(x) + \frac{t_{k+m+1}^J - x}{t_{k+m+1}^J - t_{k+1}^J} N_{J,k+1}^{m-1}(x) \quad (3.2)$$

with $m = 1, 2$ from the initial values

$$N_{J,k}^0(x) = \begin{cases} 1 & \text{if } t_k^J < x < t_{k+1}^J \text{ and } t_k^J < t_{k+1}^J \\ 0 & \text{otherwise} \end{cases};$$

see e.g. Stollnitz et al. (1995) or Schmidt (2007). The level-dependent number K_J of terms in the expansion (3.1) is defined as $K_J = 2^J + 2$. For regional modelling, we introduce the so-called endpoint-interpolating quadratic B-splines defined on the unit interval $[0, 1]$. For that purpose we set the first three knots t_k^J to the value zero and the last three knots to the value one. Hence, the level- J knot sequence for endpoint-interpolating quadratic B-splines is given as

$$0 = t_0^J = t_1^J = t_2^J < t_3^J < t_4^J < \dots < t_{K_J-1}^J < t_{K_J}^J = t_{K_J+1}^J = t_{K_J+2}^J = 1 \quad (3.3)$$

where the distance between the two neighbouring knots t_k^J and t_{k+1}^J with $k = 2, 3, \dots, K_J - 1$ is equal to $h_J = 2^{-J}$; see Stollnitz et al. (1995), Lyche and Schumaker (2001), Schmidt (2007) or Schmidt et al. (2015).

The three left panels of Fig. 3.1 show at the top the four functions $N_{1,0}^2(x)$, $N_{1,1}^2(x)$, $N_{1,2}^2(x)$ and $N_{1,3}^2(x)$ of level $J = 1$ in blue, green, red and light blue, resp., computed from the seven knots

$$t_0^1 = t_1^1 = t_2^1 = 0, t_3^1 = 0.5, t_4^1 = t_5^1 = t_6^1 = 1 \quad (3.4)$$

indicated as blue dots. In the mid panel the 6 functions $N_{2,k}^2(x)$ for $k = 0, \dots, 5$ of level $J = 2$ are shown calculated from altogether 9 knots

$$t_0^2 = t_1^2 = t_2^2 = 0, t_3^2 = 0.25, t_4^2 = 0.50, t_5^2 = 0.75, t_6^2 = t_7^2 = t_8^2 = 1. \quad (3.5)$$

The bottom panel, finally, illustrates the 10 functions $N_{3,k}^2(x)$ for $k = 0, \dots, 9$ of level $J = 3$ computed from altogether 13 knots

$$\begin{aligned} t_0^3 = t_1^3 = t_2^3 = 0, t_3^3 = 0.125, t_4^3 = 0.250, t_5^3 = 0.375, t_6^3 = 0.500, \\ t_7^3 = 0.625, t_8^3 = 0.750, t_9^3 = 0.825, t_{10}^3 = t_{11}^3 = t_{12}^3 = 1. \end{aligned} \quad (3.6)$$

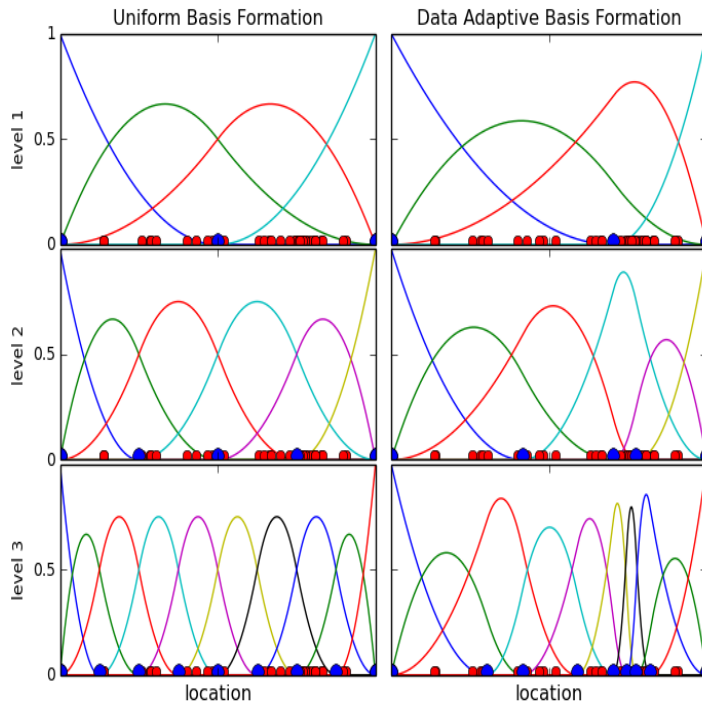


Figure 3.1: Data-adaptive basis formations of the UBS (left panels) from different B-spline levels compared to the corresponding formations set up by the NABS (right panels). The red dots indicate the observation locations whereas the blue dots are the knots which are used to create the B-spline functions.

Since the distances between the neighbouring knots are constant, the functions in the left panels of Fig. 3.1 are denoted as Uniform B-Splines (UBS). Their shapes are totally independent on the locations of the observations which are marked by the red dots.

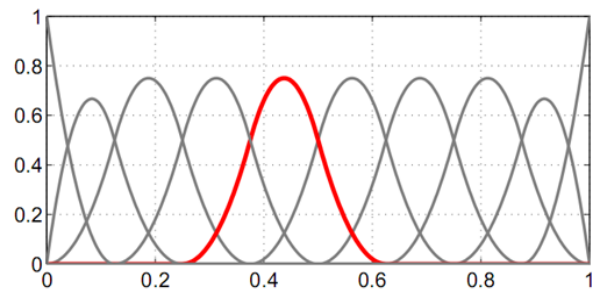
The normalized quadratic B-spline functions $N_{J,k}^2(x)$ will be used for modelling the latitude dependency of the global model part $VTEC_{\text{glob}}(\varphi, \lambda)$ introduced in Eq. (1.6). Since the latitude φ is defined within the interval $[-90^\circ, 90^\circ]$ along a meridian between the South and North Pole, the transformation formula

$$x = \frac{\varphi + 90^\circ}{180^\circ} \quad (3.7)$$

for $x \in [0, 1]$ and $\varphi \in [-90^\circ, 90^\circ]$ has to be considered before evaluating Eq. (3.2). Figure 3.2 shows another example of endpoint-interpolating B-spline functions for level $J = 3$

Figure 3.2: Normalized endpoint-interpolating quadratic B-spline functions (3.2) for level $J = 3$.

The set consists of $K_3 = 2^3 + 2 = 10$ B-spline functions. It can be seen from the red-coloured curve that each B-spline is compactly supported, i.e. it is different from zero only a small part of the domain. Furthermore, it can be seen that the first two and the last two B-spline functions are modified by the endpoint-interpolating procedure; for more details see Schmidt (2007).



Besides the normalized quadratic B-spline functions $N_{J,k}^2(x)$ we also introduce the normalized periodic trigonometric B-splines $T_{J,k}^2(y)$ of order 2 for level $J \in \mathbb{N}_0$ and shift $k = 0, 1, \dots, \tilde{K}_J - 1$ depending on

the variable $y \in [0, 2\pi]$. Recurrence relations for calculating the periodic trigonometric B-splines from the initial trigonometric B-splines $T_{j,k}^1(y)$ of order 1 are presented, e.g. by Schumaker and Traas (1991) or Schmidt et al. (2015) and will not be repeated here. The corresponding series expansion for a function $g(y)$ reads

$$g(y) = \sum_{k=0}^{\tilde{K}_J-1} \tilde{d}_{j,k} T_{j,k}^2(y). \quad (3.8)$$

The number \tilde{K}_J of trigonometric B-spline functions $T_{j,k}^2(y)$ is defined as $\tilde{K}_J = 3 \cdot 2^J$, the distance between two neighbouring knots in the UBS case is given as $\tilde{h}_j = 2\pi \cdot 2^{-J}$; see Lyche and Schumaker (2001) or Schmidt et al. (2015).

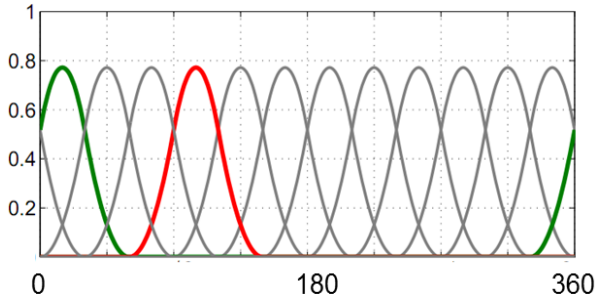


Figure 3.3: Set of $\tilde{K}_2 = 3 \cdot 2^2 = 12$ trigonometric B-spline functions $T_{j,k}^2$ for $J = 2$. The red-coloured curve shows the the basis function $T_{2,2}^2$. The green-coloured curves mean the non-zero part of $T_{2,11}^2$ and show the "wrap-around" effect.

The trigonometric B-spline functions $T_{j,k}^2(y)$ will be used for modelling the longitude dependency of the global model part $VTEC_{\text{glob}}(\varphi, \lambda)$ introduced in Eq. (1.6). Since the longitude λ is defined within the interval $[0^\circ, 360^\circ]$ along a circle of latitude, the transformation formula

$$y = \lambda \frac{\pi}{180^\circ} \quad (3.9)$$

for $y \in [0, 2\pi]$ and $\lambda \in [0^\circ, 360^\circ]$ has to be considered. In addition, the trigonometric B-splines have to be periodic along the equator, such that the so-called "wrap-around" effect holds. As can be seen from Fig. 3.3 this effect is automatically included in the definition of the trigonometric B-spline functions as discussed by Schmidt et al. (2015). In this case no additional constraint has to be considered.

3.2 1-dimensional modelling with Non-Uniform Adaptive B-Splines (NABS)

As mentioned before UBS do not consider the distribution of the data, i.e. the spatial locations of the observations, as can be seen from Fig. 3.1. However, since a denser distribution of the observation sites allows the modelling of finer structures, i.e. a higher frequency part of the signal under investigation, more and sharper B-spline functions should be placed within this region. Thus, we would like to increase the number of B-splines in the right part of the shown interval along the x -axis in Fig. 3.1. In other words, the locations of the B-spline functions shall be adapted to the data locations, i.e. the distribution. The so-called Non-uniform Adaptive B-Spline (NABS) functions allow such a representation. For that purpose we keep the series expansion and just modify the locations of the knots as defined in Eq. (3.3).

To be more specific, we assume that observations are given at arbitrary distributed N locations $x_1, x_2, \dots, x_i, \dots, x_N$ within the unit interval $[0, 1]$. For a data-adaptive distribution of the knots t_k^J as introduced in Eq. (3.2) for level $J = 1$ we define the knot t_3^1 according to

$$t_3^1 = \frac{1}{N} \sum_{i=1}^N x_i \quad (3.10)$$

as the average of the N locations. The top panel of the right side of Fig. 3.1 shows this knot location as a blue dot. Substituting the right-hand side of Eq. (3.10) for the value 0.5 in Eq. (3.4) and introducing

the resulting seven knots in Eq. (3.2) the four normalized quadratic B-spline functions $N_{1,k}^2(x)$ as shown in the top right panel of Fig. 3.1 are computable. Since their locations and their shapes are adapted to the data distribution the term “Non-uniform Adaptive B-Spline” (NABS) was chosen.

In the next step, i.e. for level $J = 2$, we collect the number $N_{x_i \in X_1}$ of observation locations with $x_i \leq t_3^1$ in the set X_1 and compute the knot t_3^2 as their average value, i.e.

$$t_3^2 = \frac{1}{N_{x_i \in X_1}} \sum_{i=1}^{N_{x_i \in X_1}} x_i . \quad (3.11)$$

In the same manner we collect the $N_{x_i \in X_2}$ observation locations with $x_i > t_3^1$ in the set X_2 and compute the knot location

$$t_5^2 = \frac{1}{N_{x_i \in X_2}} \sum_{i=1}^{N_{x_i \in X_2}} x_i \quad (3.12)$$

with $N_{x_i \in X_2} = N - N_{x_i \in X_1}$. Together with the knot location $t_5^2 = t_3^1$ from Eq. (3.10) we obtain the values of the three central knots of level $J = 2$ as in Eq. (3.5), but now for the NABS formation. Introducing these knots together with the unchanged ones for the left and the right boundary of the unit interval we can compute the normalized quadratic B-spline functions $N_{2,k}^2(x)$ from Eq. (3.2). These $K_2 = 2^2 + 2 = 6$ NABS are shown in the mid panel on the right side of Fig. 3.1. In the same way, we computed the knots and the altogether 10 NABS functions of level $J = 3$ visualized in the bottom panel. As an alternative to the method we described before the median can be chosen. In this case Eq. (3.10) is replaced by

$$t_3^1 = \text{med}(x_1, x_2, \dots, x_N) .$$

Similar equations follow for the computation of the knot locations t_3^2 and t_5^2 for level $J = 2$.

3.3 2-dimensional global modelling with UBS and NABS

In ionosphere modelling in the Sun-fixed coordinate system a 2-D spatial function $f(x, y)$ given globally on a sphere Ω with radius R is traditionally represented by a series expansion in spherical harmonics (SH); see e.g. Schaer (1999). Since SHs are oscillating over the whole sphere, and thus, characterized by a global behaviour, they cannot represent data of heterogeneous density and quality in a proper way as already mentioned before and shown in Fig. 2.2 (Schmidt et al., 2011). Figure 3.4 visualizes the distribution of the global IGS stations.

As an alternative to the SH expansion we introduce the 2-D series expansion

$$f(x, y) = \sum_{k_1=0}^{K_{J_1}-1} \sum_{k_2=0}^{K_{J_2}-1} d_{k_1, k_2}^{J_1, J_2} \Phi_{k_1, k_2}^{J_1, J_2}(x, y) \quad (3.13)$$

in terms of the 2-D basis functions $\Phi_{k_1, k_2}^{J_1, J_2}(x, y)$. In the following we identify the function $f(x, y)$ with the global $VTEC_{\text{glob}}(\varphi, \lambda)$ signal as introduced in Eq. (1.5). Furthermore, the 2-D basis functions are defined as the tensor product of the normalized quadratic B-spline functions $N_{J_1, k_1}^2(x)$ and the trigonometric B-spline functions $T_{J_2, k_2}^2(y)$, i.e.

$$VTEC_{\text{glob}}(\varphi, \lambda) = \sum_{k_1=0}^{K_{J_1}-1} \sum_{k_2=0}^{K_{J_2}-1} d_{k_1, k_2}^{J_1, J_2} N_{J_1, k_1}^2(\varphi) T_{J_2, k_2}^2(\lambda) . \quad (3.14)$$

The initially unknown $K_{J_1} \cdot K_{J_2}$ series coefficients $d_{k_1, k_2}^{J_1, J_2}$ have to be computed together with other unknown parameters by parameter estimation from the GNSS NRT observations defined in Eq. (2.4).



Figure 3.4: IGS network with globally distributed stations with high coverage over Europe and huge data gaps over the oceans. However, meanwhile several islands are worldwide equipped with GNSS receiver stations.

It has to be mentioned that Eq. (3.14) will be evaluated within the Sun-fixed Geocentric Solar Magnetic (GSM) coordinate system. It is usually defined for high altitudes in regions which are strongly influenced by the solar wind and the interplanetary magnetic field (Laundal and Richmond, 2017). The x -axis of the GSM is pointing from the geocentre to the Sun. The y -axis is perpendicular to the magnetic dipole axis and the Earth-Sun line. The positive direction of the system is pointing towards the dusk. The z -axis is completing the right-handed system in the plane containing the Earth-Sun line and the dipole axis. The transformation equation between the geographical coordinate system and the GSM coordinate system is described by Hapgood (1992).

Figure 3.5 shows exemplarily the global distribution of $(K_{J_1} = 10) \times (K_{J_2} = 12) = 120$ tensor products $N_{J_1, k_1}^2(\varphi) \cdot T_{J_2, k_2}^2(\lambda)$, which are the 2-D basis functions defined in the plane spanned by longitude λ and latitude φ . The approximation quality of the B-spline representations (UBS and NABS) is depending on the values K_{J_1} and K_{J_2} and, thus, on the levels J_1 and J_2 . The inequalities

$$J_1 \leq \log_2 \left(\frac{\pi}{\Delta\varphi} - 1 \right) \leq \log_2 (n_{\varphi, \max} - 1), \quad (3.15)$$

$$J_2 \leq \log_2 \left(\frac{2\pi}{3 \Delta\lambda} \right) \leq \log_2 \left(\frac{2n_{\lambda, \max}}{3} \right), \quad (3.16)$$

relate on the left side the averaged sampling or resolution intervals $\Delta\varphi$ and $\Delta\lambda$ of the observations in longitudinal and latitudinal direction to the level values J_1 and J_2 . On the right side the relations to the spectral degree values $n_{\varphi, \max}$ and $n_{\lambda, \max}$ of a global VTEC representation in SHs are realized.

The IGS VTEC maps are usually the result of series expansions in SHs up to degree and order $n = n_{\max} = 15$. The relations between the resolution intervals $\Delta\varphi$ and $\Delta\lambda$ of the observations and the maximum degree n_{\max} are presented in the right parts of (3.15) and (3.16). However, it must be noted that in the given case the maximum values $n_{\varphi, \max}$ in latitude direction can differ from the corresponding value $n_{\lambda, \max}$ in longitude direction. As maximum value n_{\max} the smaller one of the two degree values $n_{\varphi, \max}$ and $n_{\lambda, \max}$ is chosen. Thus, taken the value $n_{\max} = 15$ into account, we estimated the level values in Eq. (3.14) from the inequalities (3.15) and (3.16) to $J_1 = 4$ and $J_2 = 3$. Consequently,

$(K_{J_1} = 18) \times (K_{J_2} = 24) = 432$ series coefficients $d_{k_1, k_2}^{4,3}$ must be determined by parameter estimation from NRT GNSS observations. This issue will be discussed in Section 4.

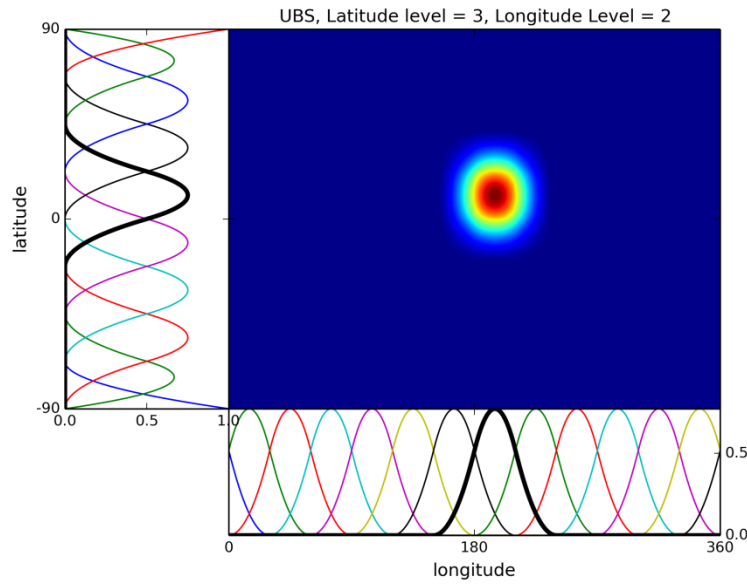


Figure 3.5: Distribution of the 2-D tensor products of normalized quadratic B-spline functions and trigonometric B-spline functions of the levels $J_1 = 3$ in latitude direction and $J_2 = 2$ in longitude direction. The tensor product of the two spline functions highlighted in black yields the shown 2-D function, as an example of a UBS function. Whereas in the 2-D representation light blue means a small positive value, the dark red colour represents the largest magnitude of up to value 1.

To consider the time-dependency of the VTEC values the series expansion is extended to consider time series for the set of coefficients $d_{k_1, k_2}^{J_1, J_2}$ through

$$VTEC_{\text{glob}}(\varphi, \lambda, t) = \sum_{k_1=0}^{K_{J_1}-1} \sum_{k_2=0}^{K_{J_2}-1} d_{k_1, k_2}^{J_1, J_2}(t) N_{J_1, k_1}^2(\varphi) T_{J_2, k_2}^2(\lambda). \quad (3.17)$$

Herein the coefficients are estimated by Kalman filtering and forecasted by deterministic Fourier series expansions and stochastic processes such as autoregressive and moving average (ARMA) models as will be discussed in Subsection 3.5.

3.4 2-dimensional regional modelling with UBS and NABS

In certain regions such as Europe, North America, Japan or parts of South America, regional GNSS data exist, partly in NRT or even in RT which could be used for a regional densification. To be more specific, we assume that within a rectangular area $\Delta\Omega$ of size $\Phi \times \Lambda$ high-resolution GNSS observations in RT is available. Here we assume that Φ is the extension of the area with respect to the geographical latitude and Λ the stretch of $\Delta\Omega$ with respect to the geographical longitude. Note, whereas the global model is defined within the GSM coordinate system, the regional model is related to the geographical coordinate systems. Furthermore, we assume that the sampling intervals $\Delta\varphi$ and $\Delta\lambda$ allow a high-frequency modelling. If the size of the area and the sampling intervals are given, the right parts of the inequality equations (3.15) and (3.16) allow for the computation of the maximum degree n_{max} for the spectral modelling of VTEC in SHs, which should clearly exceeds the degree 15.

The model for the high-resolution ionosphere variations $\Delta VTEC$ within the densification area, i.e. $\Delta VTEC_{\text{reg}}$ as introduced in Eq. (1.6), is set up as a 2-D series expansion in terms of tensor products of the normalized quadratic B-spline functions $N_{J, k}^2(x)$ with respect to latitude and longitude, i.e.

$$\Delta VTEC_{\text{reg}}(\varphi, \lambda, t) = \sum_{k_3=0}^{K_{J_3}-1} \sum_{k_4=0}^{K_{J_4}-1} d_{k_3, k_4}^{J_3, J_4}(t) N_{J_3, k_3}^2(\varphi) N_{J_4, k_4}^2(\lambda) \quad \forall P(\varphi, \lambda) \in \Delta\Omega. \quad (3.18)$$

In opposite to the left-hand parts of the Eqs. (3.15) and (3.16) in regional applications the two level values J_3 and J_4 are calculable from the inequality relations

$$J_3 \leq \log_2 \left(\frac{\Phi}{\Delta\varphi} - 1 \right), \quad (3.19)$$

$$J_4 \leq \log_2 \left(\frac{\Lambda}{\Delta\lambda} - 1 \right). \quad (3.20)$$

The most important point in the determination of the level values J_3 and J_4 is the spectral connection of the global and the regional model part. To be more specific, the smallest wavelength of the global model must be shorter or equal than the largest one of the regional model. Following the approximation formula $L_{\min} \approx 2\pi R/n_{\max}$ we obtain for $n_{\max} = 15$ a minimum length of $L_{\min} = 2670$ km which corresponds to a spherical extension of approximately 24° on a sphere Ω with radius $R = 6370$ km. Consequently, we chose for the area of investigation, i.e. the densification area $\Delta\Omega$ an extension of $\Phi = 30^\circ$ along the geographical meridian and $\Lambda = 40^\circ$ along the geographical equator and its parallels. With given numerical values for the average sampling intervals $\Delta\lambda$ and $\Delta\varphi$ we apply the inequalities (3.19) and (3.20) and obtain the level values J_3 and J_4 .

Equation (3.18) can be used for the representation of the regional $\Delta VTEC$ variations in terms of both UBS and NABS functions for the level values J_3 and J_4 .

3.5 Forecast model for the global UBS coefficients

An approach based on a time series analysis of the VTEC model has been developed to obtain a prediction of VTEC for the time difference between RT and NRT. In our understanding, this time difference will amount at most three hours. The method should be as precise as possible, since the ionospheric state may change very fast. Thus, our model consists of a deterministic and a stochastic part and is applied to the B-spline coefficients $d_{k_1, k_2}^{J_1, J_2}(t)$ of the global model (3.17). To be more specific, we model the time dependency of each coefficient as

$$d_{k_1, k_2}^{J_1, J_2}(t) = (a_0 + \sum_{i=1}^n \{a_i \cos(\omega_i t) + b_i \sin(\omega_i t)\})_{k_1, k_2} + s_{k_1, k_2}(t), \quad (3.21)$$

i.e. as the sum of a Fourier series with given angular frequencies $\omega_i = 2\pi/T_i$ and a stochastic part $s_{k_1, k_2}(t)$, e.g. an ARMA model. We applied a Fourier analysis to determine the most important signal component, namely for the periods $T_1 = 1$ day, $T_2 = 0.5$ day, $T_3 = 0.33$ day, $T_4 = 0.25$ day and so on. In addition we consider oscillations with periods of $T_i = 15$ minutes. Note, the coefficients a_0 , a_i and b_i for $i = 1, \dots, n$ are estimated for each coefficient $d_{k_1, k_2}^{J_1, J_2}$ independently by evaluating its time series over the five previous days. Once the coefficients are estimated, forecasted VTEC values $\widehat{VTEC}_{\text{fglob}}$ can be obtained by extrapolating Eq. (3.21) to the present time and be used in RT applications (see Fig. 3.6).

Note, that the Eq. (3.21) can be easily applied to the set of coefficients $d_{k_1, k_2}^{J_1, J_2}(t)$ in the UBS case, since the geographical locations – depending on the index pair (k_1, k_2) – of the coefficients are stationary. In the NABS case, however, these locations are weakly non-stationary.

3.6 Combination of global and regional VTEC representation

Taken the conclusions of the previous subsections into account our densification approach consists of a global model part given by Eq. (3.17) and a regional model part as described in Eq. (3.18). In the first step, i.e. for the computation of the global model part we chose as basis functions 2-D tensor products of normalized quadratic B-spline functions $N_{J_1, k_1}^2(\varphi)$ and trigonometric B-spline functions $T_{J_2, k_2}^2(\lambda)$ of resolution levels $J_1 = 4$ and $J_2 = 3$ in UBS formation defined in the GSM coordinate system as will be discussed in Section 5. The altogether 432 series coefficients $d_{k_1, k_2}^{4,3}(t)$ are computed from NRT observations $\tilde{L}_{r, NRT}^s$ from GPS and GLONASS within a Kalman filtering procedure. In the second step of the procedure the reduced RT observations

$$\tilde{L}_{r, RT}^s - \alpha \cdot m(z) \cdot \widehat{VTEC}_{f_{\text{glob}}}(\varphi, \lambda, t) =: \bar{L}_{r, RT}^s \quad (3.22)$$

are chosen. Herein the value $\widehat{VTEC}_{f_{\text{glob}}}(\varphi, \lambda, t)$ is the estimated VTEC value from the forecast model evaluated at the regional observation site $P(\varphi, \lambda) \in \Delta\Omega$ from the reference time moment of the global forecast model to the time moment t of the RT observation $\tilde{L}_{r, RT}^s$ according to Eq. (3.21).

Figure 3.6 shows the basic steps of the procedure

$$VTEC_{\text{reg}}(\varphi, \lambda) = \underbrace{VTEC_{\text{glob}}(\varphi, \lambda)}_{\text{1st step}} + \underbrace{\Delta VTEC_{\text{reg}}(\varphi, \lambda)}_{\text{2nd step}}. \quad (3.23)$$

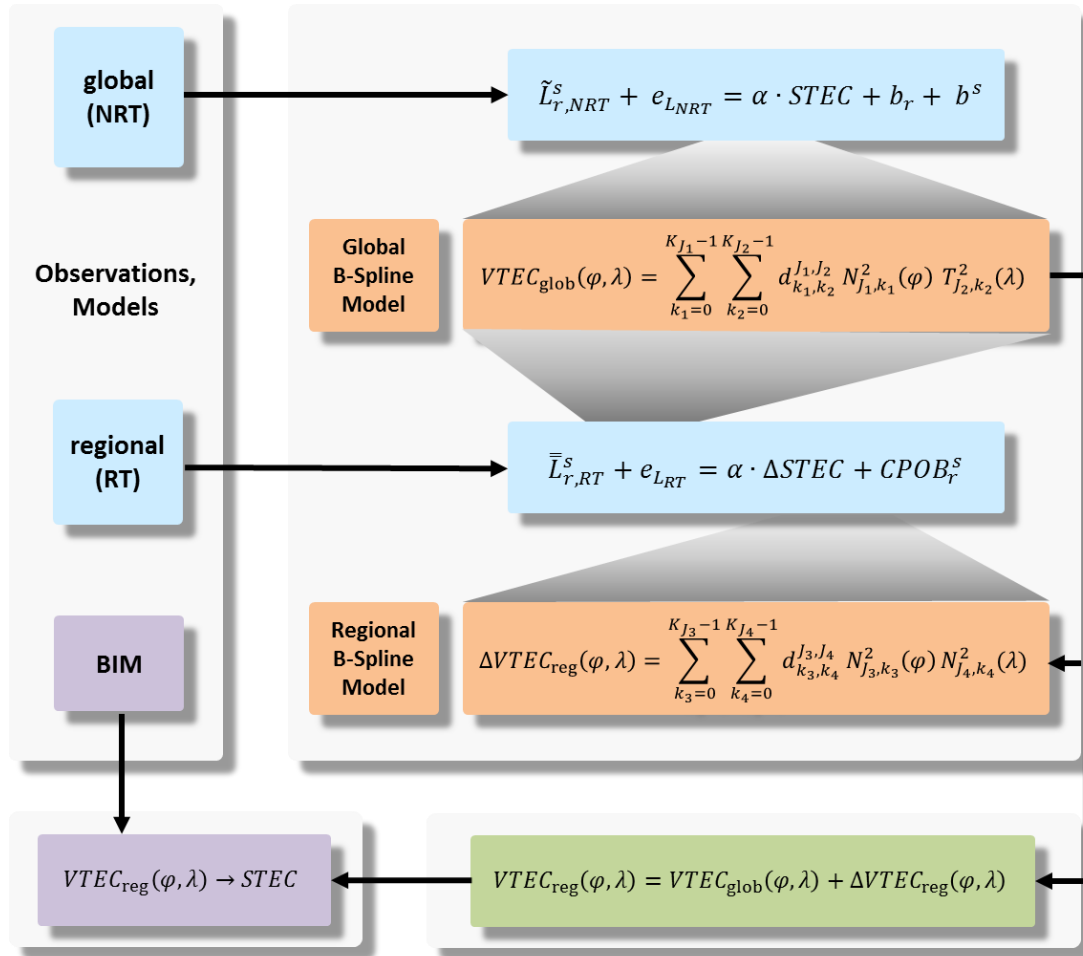


Figure 3.6: Flowchart of the developed densification approach by combining a global B-spline model, estimated from global observations $\tilde{L}_{r, NRT}^s$, and a regional densification B-spline model computed from the regional observations $\tilde{L}_{r, RT}^s$.

4. Concept of the high-resolution real-time VTEC model for selected densification areas

Introduction

The procedures related with ionospheric data processing and filtering as well as the overall concept, which is necessary for developing the regional VTEC modelling approach in the area of investigation, e.g. parts of Europe, are explained in the following subsections.

4.1 Observation equations

Throughout this project, GPS and GLONASS data have been used to estimate global and regional VTEC maps. The observation equations are already shown in Figure 3.6 for the global NRT and the regional RT observations. It should be noted that these equations need to be split into a GPS and a GLONASS part in order to deal with the different biases related to both techniques and the different accuracies, namely

$$\tilde{L}_{r,NRT}^{GPS} + e_{GPS} = \alpha \cdot m(z) \cdot VTEC_{glob} + b_{r,GPS} + b_{GPS}^s \quad (4.1a)$$

$$\tilde{L}_{r,NRT}^{GLO} + e_{GLO} = \alpha \cdot m(z) \cdot VTEC_{glob} + b_{r,GLO} + b_{GLO}^s \quad (4.1b)$$

where $\tilde{L}_{r,NRT}^{GPS}$ and $\tilde{L}_{r,NRT}^{GLO}$ are the global NRT observables from Eq. (2.4) under the consideration of the mapping function (1.5). For the regional densification model part we have to establish the observation equations for the reduced RT observations $\bar{L}_{r,RT}^{GPS}$ and $\bar{L}_{r,RT}^{GLO}$ according to Eq. (3.22). The corresponding observation equations read

$$\bar{L}_{r,RT}^{GPS} + \bar{e}_{GPS} = \alpha \cdot m(z) \cdot \Delta VTEC_{reg} + CPOB_{r,GPS}^s \quad (4.2a)$$

$$\bar{L}_{r,RT}^{GLO} + \bar{e}_{GLO} = \alpha \cdot m(z) \cdot \Delta VTEC_{reg} + CPOB_{r,GLO}^s \quad (4.2b)$$

where $\Delta VTEC_{reg}$ could be represented by Eq. (3.18). From the Eqs. (4.1a,b) and (4.2a,b) we define the observation vectors $\tilde{\mathbf{y}}_{GPS} = (\tilde{L}_{r,NRT}^{GPS})$, $\tilde{\mathbf{y}}_{GLO} = (\tilde{L}_{r,NRT}^{GLO})$, $\bar{\mathbf{y}}_{GPS} = (\bar{L}_{r,RT}^{GPS})$ and $\bar{\mathbf{y}}_{GLO} = (\bar{L}_{r,RT}^{GLO})$ as well as the corresponding error vectors $\tilde{\mathbf{e}}_{GPS}$, $\tilde{\mathbf{e}}_{GLO}$, $\bar{\mathbf{e}}_{GPS}$, $\bar{\mathbf{e}}_{GLO}$. Furthermore we introduce the vectors $\mathbf{d}_{J_1,J_2} = (d_{k_1,k_2}^{J_1,J_2})$, $\mathbf{d}_{J_3,J_4} = (d_{k_3,k_4}^{J_3,J_4})$ of B-spline coefficients for the global and the regional model part, respectively, and the vectors $\mathbf{b}_{GPS} = (b_{r,GPS})$, $\mathbf{b}_{GLO} = (b_{r,GLO})$ of the receiver DCBs and $\mathbf{b}^{GPS} = (b_{GPS}^s)$, $\mathbf{b}^{GLO} = (b_{GLO}^s)$ of the satellite DCBs. Finally, we define the vectors \mathbf{b}_{CPOB}^{GPS} and \mathbf{b}_{CPOB}^{GLO} of the unknown receiver-satellite pair CPOB biases.

From the observation equations (4.1a,b) und (4.2a,b) we set up the Gauß-Markov model

$$\mathbf{y} + \mathbf{e} = \mathbf{X}\boldsymbol{\beta} \quad \text{with} \quad E(\mathbf{e}) = \mathbf{0} \quad \text{and} \quad D(\mathbf{y}) = \boldsymbol{\Sigma}_y = \sigma_y^2 \mathbf{P}_y^{-1} \quad (4.3)$$

(Koch, 1999) with the measurement vector \mathbf{y} , the measurement error vector \mathbf{e} , the coefficient matrix \mathbf{X} , the vector $\boldsymbol{\beta}$ of the unknown parameters, the given positive definite weight matrix \mathbf{P}_y and the unknown variance factor σ_y^2 .

To be more specific, we define for the global model according to the Eqs. (4.1a,b)

$$\mathbf{y} = \begin{bmatrix} \tilde{\mathbf{y}}_{GPS} \\ \tilde{\mathbf{y}}_{GLO} \end{bmatrix}, \boldsymbol{\beta} = \begin{bmatrix} \mathbf{d}_{J_1, J_2} \\ \mathbf{b}^{GPS} \\ \mathbf{b}_{GPS} \\ \mathbf{b}^{GLO} \\ \mathbf{b}_{GLO} \end{bmatrix}, \boldsymbol{\Sigma}_y = \begin{bmatrix} \boldsymbol{\Sigma}_{GPS} & \mathbf{0} \\ \mathbf{0} & \boldsymbol{\Sigma}_{GLO} \end{bmatrix} \quad (4.4a)$$

where $\boldsymbol{\Sigma}_{GPS} = \sigma_{GPS}^2 \mathbf{P}_{GPS}^{-1}$ and $\boldsymbol{\Sigma}_{GLO} = \sigma_{GLO}^2 \mathbf{P}_{GLO}^{-1}$ mean positive definite covariance matrices of the GPS and the GLONASS observations; $\mathbf{0}$ is a zero matrix of an appropriate size. Correspondingly, to Eq. (4.4a) we define for the regional densification model according to the Eqs. (4.2a,b)

$$\mathbf{y} = \begin{bmatrix} \bar{\mathbf{y}}_{GPS} \\ \bar{\mathbf{y}}_{GLO} \end{bmatrix}, \boldsymbol{\beta} = \begin{bmatrix} \mathbf{d}_{J_3, J_4} \\ \mathbf{b}_{CPOB}^{GPS} \\ \mathbf{b}_{CPOB}^{GLO} \end{bmatrix}, \boldsymbol{\Sigma}_y = \begin{bmatrix} \boldsymbol{\Sigma}_{GPS} & \mathbf{0} \\ \mathbf{0} & \boldsymbol{\Sigma}_{GLO} \end{bmatrix}. \quad (4.4b)$$

The design matrix \mathbf{X} is built up accordingly and contains amongst other elements the B-spline basis functions.

It must be mentioned that RT observations introduce one additional unknown parameter for each receiver-satellite pair, since the modelling approach is based on carrier phase observations. Therefore, to decrease the number of unknowns in the state vector for the RT modelling, only GPS observables are considered.

4.2 Filter prediction model

VTEC exhibits a time varying phenomenon. Therefore, a proper model is required to take the time variation of the ionospheric parameters into account. In the NRT modelling VTEC is represented in the GSM coordinate system which results in much slower variations of the B-spline coefficients in time. Moreover, the satellite and receiver DCBs vary very slowly. Therefore, a random walk approach is performed for all the unknown parameters for the NRT model part.

The RT approach is set up in an Earth-fixed geographical coordinate system. Although VTEC varies significantly faster in this coordinates system, the main part of the VTEC trend is represented by the forecast model which acts as a background model. The estimated differences of VTEC with respect to the forecasted VTEC values, i.e. $\Delta VTEC_{reg}$, exhibit much slower time variations. Additionally, the phase biases in the unknown state vector are constant during phase continuous arcs. Consequently, the random walk approach is also considered as prediction model for the unknown target parameters of the regional RT modelling approach.

4.3 Sequential Kalman Filtering

The Kalman-Filter (KF, Kalman, 1960) is a sequential estimator which yields the ionospheric parameters according to Fig. 3.6 in NRT (global part) and in RT (regional part). In the KF the input data from the past have not to be stored and the current state is updated as soon as new observations are available (Gelb, 1974). In RT applications, this is a crucial advantage because the filter allows assimilation of observations as soon as possible without waiting for another group of observations (see e.g., Erdogan et al., 2017).

The KF is an optimal recursive estimator in terms of minimum variance estimation including a time update (prediction step) and a measurement update (correction step); see e.g. Grewal and Andrews, 2008; Simon, 2006; Gelb 1974). The approach for the estimation of the ionospheric target parameters consists of linear equations. Therefore, in the sense of KF, the linear system of equations in discrete form is defined as

$$\boldsymbol{\beta}_k = \mathbf{F}_k \boldsymbol{\beta}_{k-1} + \boldsymbol{\omega}_{k-1} \quad (4.5a)$$

$$\mathbf{y}_k = \mathbf{X}_k \boldsymbol{\beta}_k + \mathbf{e}_k \quad (4.5b)$$

where $k = t_k$ is the time stamp, \mathbf{F}_k means the transition matrix, $\boldsymbol{\beta}_k$ is the vector of the unknown parameters, \mathbf{y}_k is the vector of the measurements and \mathbf{X}_k represents the corresponding design matrix. The vectors \mathbf{e}_k and $\boldsymbol{\omega}_k$ are the vectors of the measurement errors and the process noise, respectively, with the corresponding covariance matrices $\boldsymbol{\Sigma}_y$ and $\boldsymbol{\Sigma}_\omega$. The measurement errors and the process noise are assumed as white noise with expectation values $E(\mathbf{e}_k) = \mathbf{0}$ and $E(\boldsymbol{\omega}_k) = \mathbf{0}$, and fulfil the requirements

$$E[\boldsymbol{\omega}_k \boldsymbol{\omega}_l^T] = \boldsymbol{\Sigma}_\omega \delta_{k,l} \text{ and } E[\mathbf{e}_k \mathbf{e}_l^T] = \boldsymbol{\Sigma}_y \delta_{k,l} \quad (4.6a)$$

$$E[\boldsymbol{\omega}_k \mathbf{e}_l^T] = \mathbf{0} \quad (4.6b)$$

where $\delta_{k,l}$ is the Kronecker delta symbol which equals to 1 if $k = l$ and to 0 for $k \neq l$. From the Eq. (4.6b) it becomes clearly, that the vectors $\boldsymbol{\omega}_k$ and \mathbf{e}_l are assumed to be independent.

The solution of the prediction equation (4.5) to obtain the predicted ionospheric target parameter vector $\boldsymbol{\beta}_k^-$ and its covariance matrix $\boldsymbol{\Sigma}_{\beta,k}^-$ reads

$$\boldsymbol{\beta}_k^- = \mathbf{F}_k \widehat{\boldsymbol{\beta}}_{k-1} \quad (4.7a)$$

$$\boldsymbol{\Sigma}_{\beta,k}^- = \mathbf{F}_k \widehat{\boldsymbol{\Sigma}}_{\beta,k-1} \mathbf{F}_k^T + \boldsymbol{\Sigma}_\omega. \quad (4.7b)$$

Details on the computation of the covariance matrix $\widehat{\boldsymbol{\Sigma}}_{\beta,k-1}$ can be found in Erdogan et al. (2017). The time step from epoch $k - 1$ to the next epoch k is set to 10 minutes for NRT modelling and 20 seconds for RT modelling. Once the prediction is carried out, the predicted state vector and its covariance matrix are updated with the new allocated measurements by

$$\widehat{\boldsymbol{\beta}}_k = \boldsymbol{\beta}_k^- + \mathbf{K}_k (\mathbf{y}_k - \mathbf{X}_k \boldsymbol{\beta}_k^-) \quad (4.8a)$$

$$\widehat{\boldsymbol{\Sigma}}_{\beta,k} = (\mathbf{I} - \mathbf{K}_k \mathbf{X}_k) \boldsymbol{\Sigma}_{\beta,k}^- \quad (4.8b)$$

where $\widehat{\boldsymbol{\beta}}_k$ and $\widehat{\boldsymbol{\Sigma}}_{\beta,k}$ are the updated (corrected) state vector and its covariance matrix. \mathbf{K}_k is the Kalman gain matrix which behaves like a weighting matrix.

4.4 Overall modelling approach

The various steps of the developed approach are shown in the flowchart visualized in Fig. 4.1. The first step includes the routines for downloading raw hourly GNSS data for NRT modelling. The raw data set is pre-processed to extract the ionospheric observables (2.4); the corresponding outputs are stored into a database. The next step is the near-real time filtering of hourly data that includes the parameter estimation procedures driven by the implemented Kalman filtering according to the Eqs. (4.8a,b). The NRT modelling approach is performed with a latency of less than one and a half hour. Following the NRT filtering, at the end of every hour, the parameters of the forecast model (3.21) are estimated for each of the global B-spline coefficients. Next, the forecast model with the extrapolated parameters is utilized to establish the forecasted background VTEC model for the regional modelling.

In parallel to the NRT modelling and forecasting processes, real-time data are downloaded and data pre-processing is carried out. Real time data is downloaded in binary RTCM format using the BNC software of the Federal Agency for Cartography and Geodesy (BKG) and converted into a text format. Then, the dataset is sent to the real-time data processing module to extract the ionospheric observables (2.5). In the next step, the developed regional modelling approach is performed continuously and recursively using the Kalman filtering approach (4.8a,b) to estimate the regional target parameters, that are the regional B-spline model coefficients and the corresponding unknown bias parameters. The overall RT VTEC product generation is generally accomplished in less than 30 seconds.

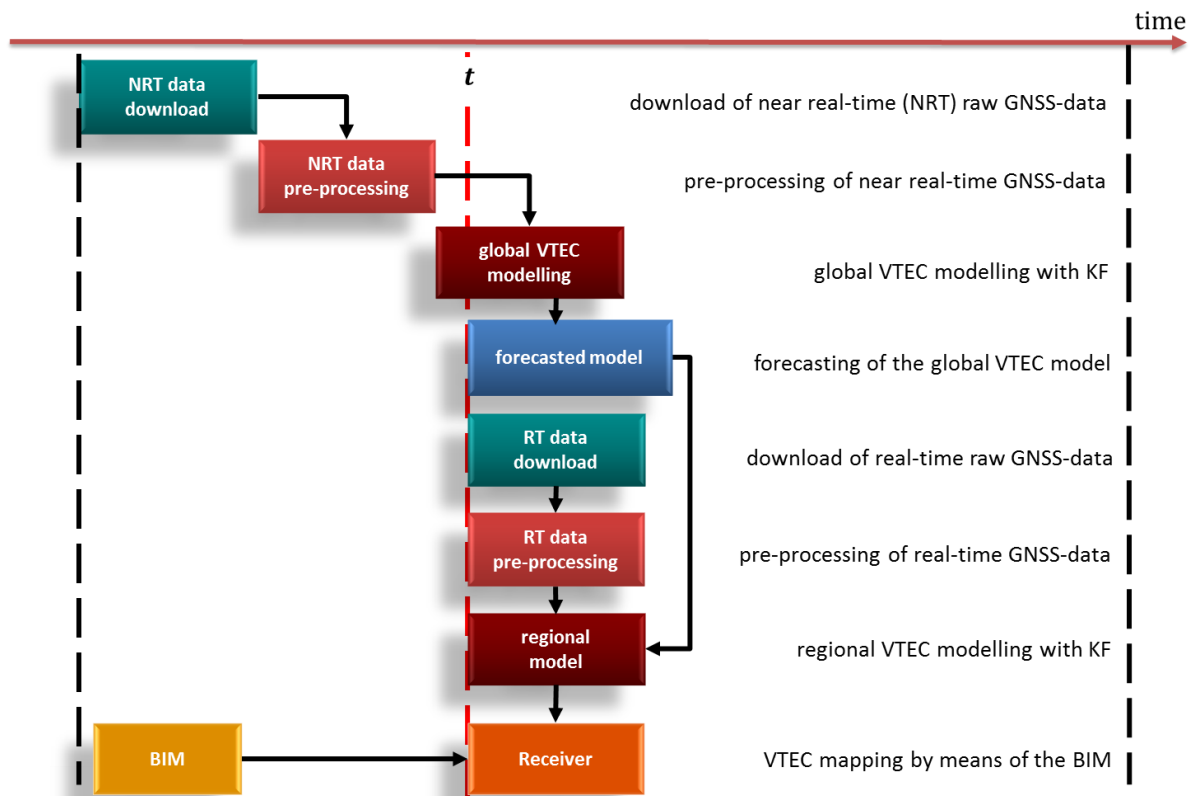


Figure 4.1: Overall flowchart of the developed NRT and RT modelling approach based on the B-spline representation

5. Numerical investigations

Introduction

Within the project AUDITOR, in particular in WP 4, great efforts have been made to study the advantages and disadvantages of the UBS and NABS series expansions for both the global and the regional application. In this sense, the following subsections are dedicated to numerical investigations which cover the screening of B-spline basis formations, the selection of appropriate resolution levels, the study of exemplified VTEC maps and of their consistency with other VTEC products provided by the IGS and its IAACs.

5.1 Global VTEC models based on UBS and NABS

As it was already mentioned in Subsection 3.2, a NABS model can be interpreted as an empirical approach, since the basis functions are directly related to the data distribution. Figure 5.1 shows, for instance, the global distributed IPPs of GNSS hourly data, i.e. the NRT input data for April 2nd, 2017, around 12:00 UTC given in the GSM coordinate system. The NABS representation for the levels $J_1 = 4$ and $J_2 = 3$, as shown in the left panel of Fig. 5.1, demonstrates that very dense knot points and steep basis function are given around Europe (yellow box in the figure) and North America. However, close to the equator, approximately between the latitudes of -30° and 30° where large VTEC gradients exist, only a small number of input data are available. Close to the North and, in particular, close to the South Pole the knot distribution is relatively sparse. The right panel of Fig. 5.1 shows the corresponding distribution of the UBS basis functions.

The characteristics of the NABS functions can be summarized as follows:

1. NABS represent regions with a higher data density by a larger number of basis functions with a narrow spatial support,
2. NABS represent regions with large data gaps by a less number of basis functions with a wide spatial support.

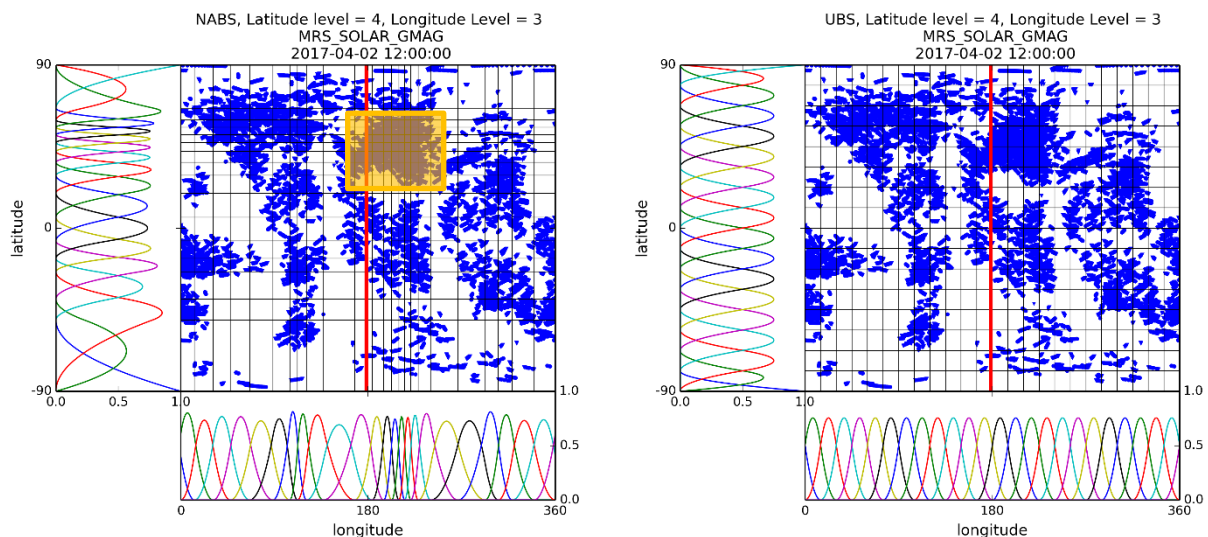


Figure 5.1: Example for the distribution of knot points and basis functions in the NABS case (left panel) and the UBS case (right panel) with resolution levels $J_1 = 4$ along latitude and $J_2 = 3$ along longitude for hourly data at 12:00 UTC on April 2nd, 2017. The red line shows the prime meridian of Greenwich.

However, often a high data density is given where the ionospheric signals are rather smooth, in particular in the mid latitudes, such as in Europe or North America. Consequently, in these areas an overfitting problem might occur, i.e. the number of B-spline terms is too large. In opposite, in areas with large

signal variations often only a few observation sites exist and, thus, the number of NABS functions is too small. We can conclude from these issues that for global modelling using NABS functions the VTEC signal structure needs to be considered in addition to the data distribution criteria.

The second issue needs to be emphasized is that the developed global modelling approach runs in NRT. As already explained in Subsection 3.5 the results of the NRT solutions are used to forecast the VTEC solution to RT. As shown in Fig. 5.2, the spatial locations and the extent of the NABS functions is varying with time. In such a case also the geographical locations of the B-spline coefficients would change with time. However, this variability does not correspond to the assumption made in Eq. (3.21). Thus, the NABS solutions cannot be used appropriately for forecasting the global VTEC model to RT.

Considering the aforementioned issues, the UBS-based VTEC representation was selected for the global modelling approach which runs in NRT whereas the NABS-based approach is preferred for the regional VTEC modelling part executed in RT. The latter procedure is explained in more detail in Subsection 5.4.

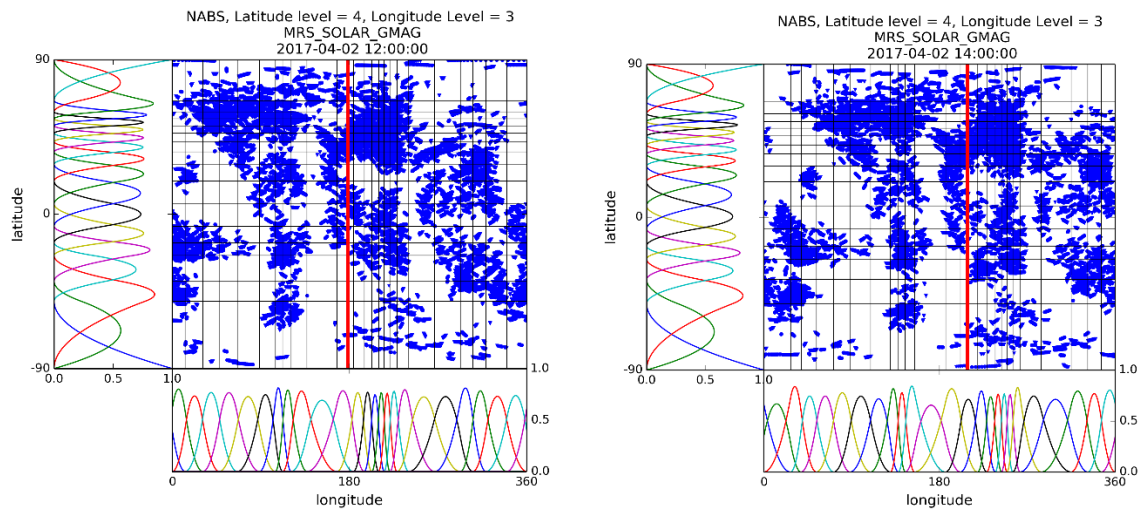


Figure 5.2: NABS-based knot point distribution and basis function formation using the resolution levels $J_1 = 4$ for latitude and $J_2 = 3$ for longitude for hourly data at 12:00 UTC (left panel) and at 14:00 UTC (right panel) on April 2nd, 2017. The red line shows the prime meridian at Greenwich. The variations of the NABS with time are clearly visible, especially w.r.t. the longitude.

5.2 Selection of global observation sites

Following the left-hand sides of the two inequalities (3.15) and (3.16) the minimum sampling intervals $\Delta\varphi$ and $\Delta\lambda$ can be computed. Based on these considerations we determined the elements of global observation vector \mathbf{y} in Eq. (4.4a) by a segmentation of the Earth's surface into bins of a size related to the sampling intervals. In the example presented in Fig. 5.3 we defined bins with a size of $10^\circ \times 10^\circ$ with respect to latitude and longitude. For all bins in which more than two NRT receiver stations of the global IGS network – with a few extensions mentioned before – are located, we selected this receiver station which is the nearest to the centre of the bin. Then all observations of the chosen receiver stations, related to the corresponding IPPs, are collected in the aforementioned vector \mathbf{y} for global modelling. Figure 5.3 shows in the left panel all available stations in NRT – with one hour latency – from the global IGS network in red. The right panel depicts the selected stations of the IGS network with a more homogeneous distribution over the globe. In addition, the left panel shows the NRT receivers of the EUREF network.

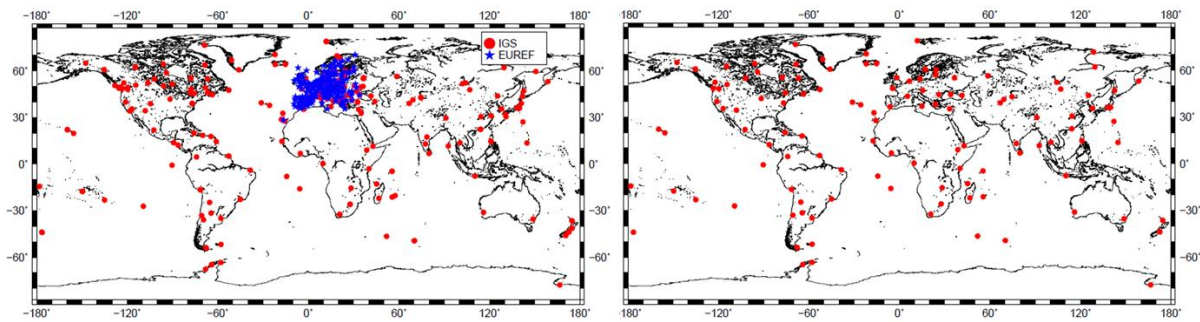


Figure 5.3: NRT receiver station positions of the IGS network in red and the NRT EUREF network in blue (left panel); selected receiver stations after the data separation based on bin segmentation with a bin size of $10^\circ \times 10^\circ$ (right panel): the observations $\tilde{L}_{T,NRT}^S$, Eq. (2.4), from the selected receiver stations are used for global modelling according to Fig. 3.6.

5.3 Overall consistency of the global VTEC maps

Numerical examples of our developed NRT model and the forecast model are compared to VTEC solutions obtained from the IGS and its IAACs to investigate the overall consistency of the solutions. In the comparisons, the label `gloUBS` and `fcUBS` refer to solutions of our NRT model and forecast model, respectively, whereas the abbreviations `igsg`, `upcg`, `codg`, `jplg` and `esag` stand for the final products of IGS and its IAACs, namely UPC, CODE, JPL and ESA – in this order.

In Figure 5.4, exemplified global VTEC maps including DGFI's NRT solution are illustrated for the epoch at 12:00 UTC on March 3rd, 2017. Moreover, the Fig. 5.5 shows the differences of the global VTEC maps, presented in Fig. 5.4, with respect to the reference map which is selected as IGS's final solution. DGFI's global NRT solution in Fig. 5.5 is in close agreement with the others in terms of the mean and the standard deviation, i.e., -1.2 and 1.3 TECU, respectively.

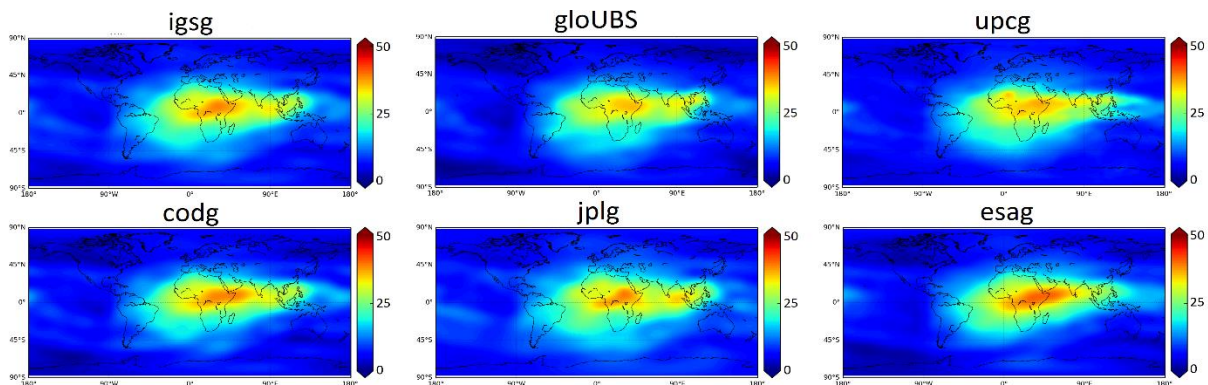


Figure 5.4: Examples of VTEC maps from IGS and its IAACs as well as the global solution of DGFI-TUM (top panel, mid column) at 12:00 UTC on March 3rd, 2017.

The analysis of the differences is extended for a one week time span covering the days between March 3rd (DOY 62) and March 10th (DOY 69), 2017. In this study, the mean value and the standard deviations of the differences, computed at each hour with respect to the reference VTEC solution are depicted in Fig. 5.6. for the entire week. The mean values vary between -2 and 1.5 TECU whereas the standard deviations range from 0.5 to 4 TECU during the week. Furthermore, to obtain an overall measure for the evaluations, the average mean values and the average standard deviations for the entire week are computed for each of the VTEC solutions and written in the parentheses on the legend of the figure. DGFI's NRT solution has an average standard deviation of 1.9 TECU which agrees well with the UPC and the ESA solutions showing a standard deviation of 1.8 TECU. The maps of the VTEC differences for CODE and JPL present very small standard deviations. This might be due to the fact that the IGS VTEC products are the combinations of both the CODE and the JPL products for the selected test period.

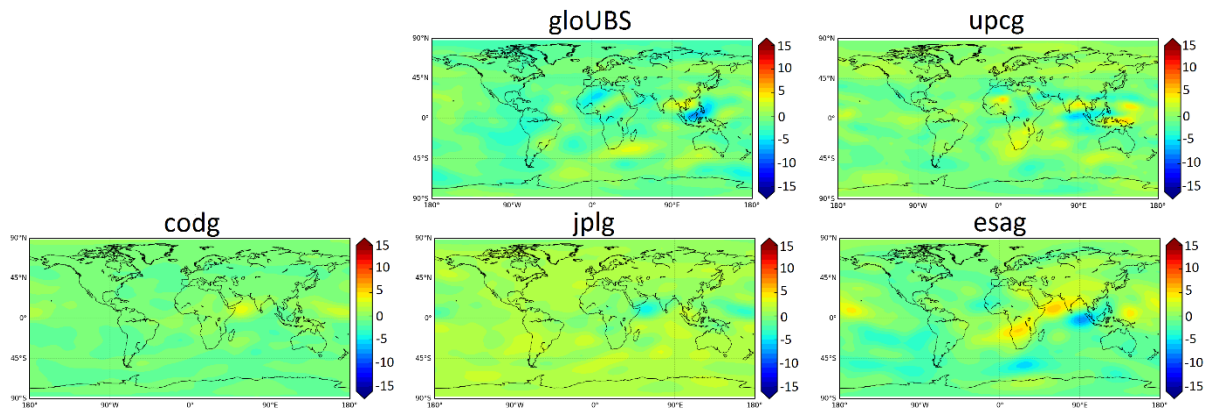


Figure 5.5: Maps of the differences between the VTEC solutions from CODE, DGFI-TUM, JPL, UPC and ESA (from left to right and top to bottom) with respect to the IGS product at 12:00 UTC on March 3rd, 2017.

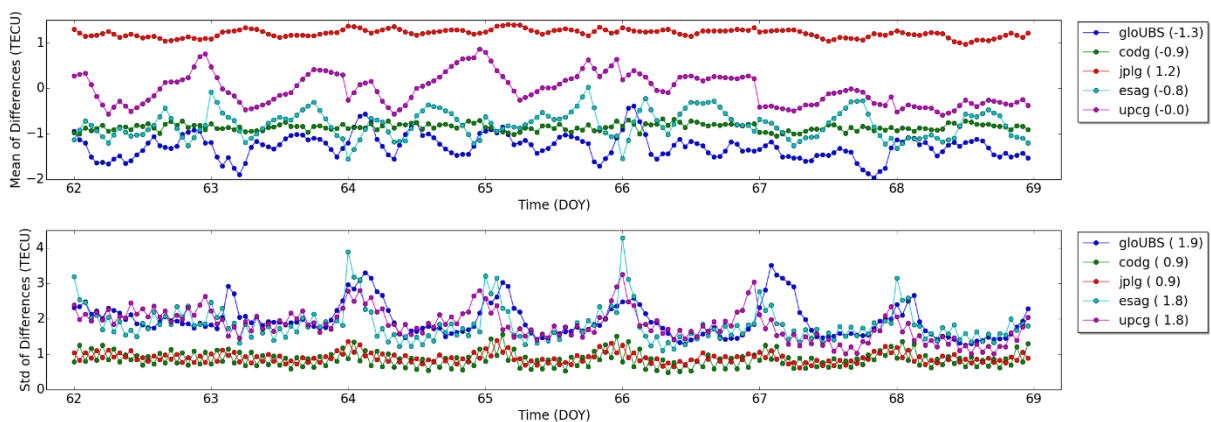


Figure 5.6: Mean values and standard deviations of the VTEC differences with respect to the IGS product.

Exemplified VTEC maps computed from the forecast model according to Eq. (3.21) are also analysed for a selected test day, namely April 2nd 2017, since our RT modelling approach for the regional densification area utilizes also the VTEC solution derived from the forecast model. However, the final VTEC product of IGS for the test day was not available on the global data server CDDIS. Therefore, the VTEC products provided by the CODE centre are considered as reference for the further evaluations. In the first row of Fig. 5.7, snapshot maps at 14:00 UTC are illustrated for the CODE centre as well as DGFI’s NRT and forecast model solutions. The differences of the DGFI solutions with respect to the CODE solution are presented in the second row of the figure. As expected the forecast model clearly shows higher differences than the NRT approach. Moreover, an average standard deviation of the difference maps for the entire day is around 3 TECU for the forecast model solution whereas the NRT solution exhibits only 2 TECU. It needs to be mentioned that the quality of the forecast solution will probably be improved by choosing a more appropriate approach for stochastic model part $s_{k_1, k_2}(t)$ in Eq. (3.21).

5.4 Regional VTEC models based on UBS and NABS

The developed final approach is based on the global NRT input data defined in Eq. (2.4) and the RT input data introduced in Eq. (2.5). To be more specific we use data acquired from the observation sites of the EUREF network in case for the regional RT modelling part to set up the observation vector \mathbf{y} as defined in Eq. (4.4b).

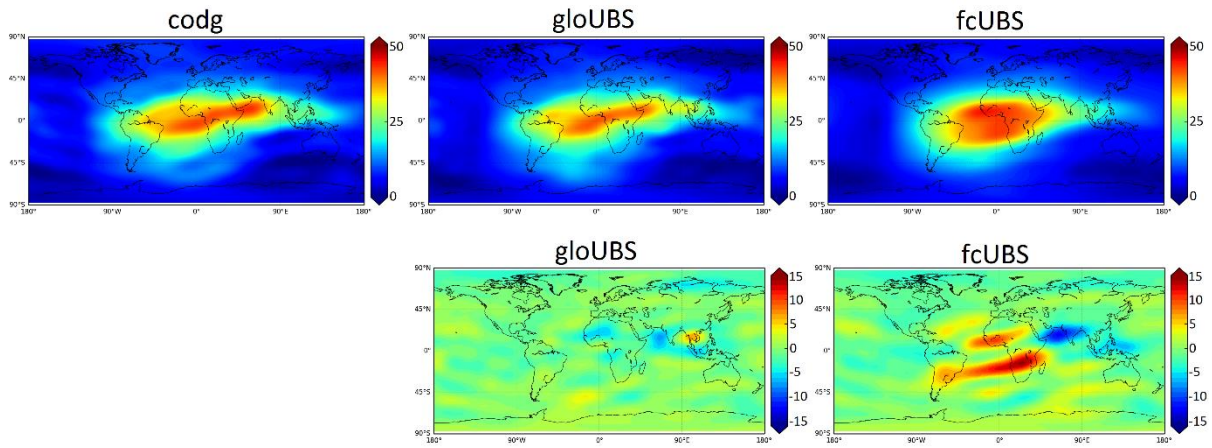


Figure 5.7: Examples of VTEC maps from CODE, DGFI's global NRT solution and the forecasted model solution based on Eq. (3.21) (first row from left to right) as well as the differences of DGFI's VTEC maps with respect to the CODE solution (second row).

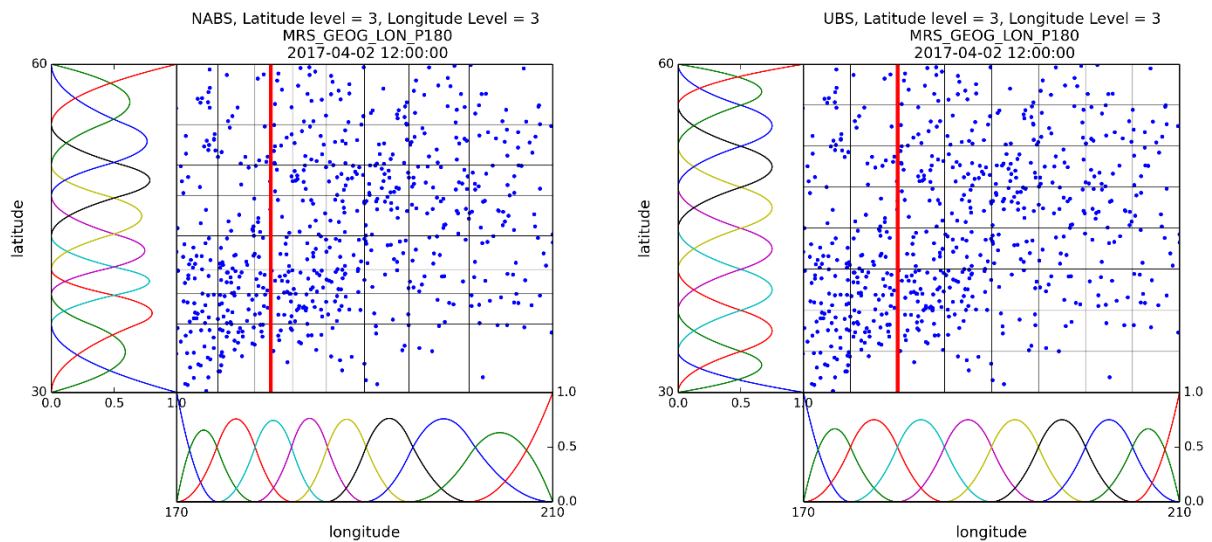


Figure 5.8: Regional distribution of NABS functions (left panel) for the RT input data (IPPs, blue dots) from the EUREF network and of UBS functions (right panel) with a regular knot distribution using the level values $J_1 = 3$ for latitude and $J_2 = 3$ for longitude at 12:00 UTC on April 2nd, 2017. The red line shows the prime meridian at Greenwich.

Figure 5.8 shows the RT data distribution and the corresponding basis formations for the NABS case (left panel) and the UBS case (right panel) at April 2nd, 2017. The level values are chosen as $J_3 = J_4 = 3$ according to the average sampling or resolution intervals as defined by the Eqs. (3.19) and (3.20). To be more specific, from Fig. 5.8 and the corresponding maps for other time moments (not shown here) we obtain for the sampling intervals of the observations $\bar{L}_{T,RT}^S$, Eq. (3.22), related to the IPPs (blue dots) the (minimum) average values $\Delta\lambda = 6.0^\circ$ and $\Delta\varphi = 4.0^\circ$. This corresponds to modelling the finer signal structures within a SH representation up to at least degree and order $n = 30$.

Figure 5.9 summarizes the overall procedure to establish regional VTEC maps following the Figs. 3.6 and 4.1. The upper left image represents the global ionospheric VTEC solution computed in NRT. Next, the part related to the area of investigation, i.e. the densification area, is forecasted to RT, i.e. to the present time moment t . The forecasted VTEC product is used as the background model $VTEC_{reg}$ in the RT approach which creates the $\Delta VTEC$ values for the densification area, which are represented by Eq. (3.18), as shown at the right side of Fig. 5.9. The final real-time VTEC product is computed by summing up the estimated regional $\Delta VTEC$ map with the background VTEC map $VTEC_{reg}$ derived from the forecast model as illustrated at the bottom-left of the figure.

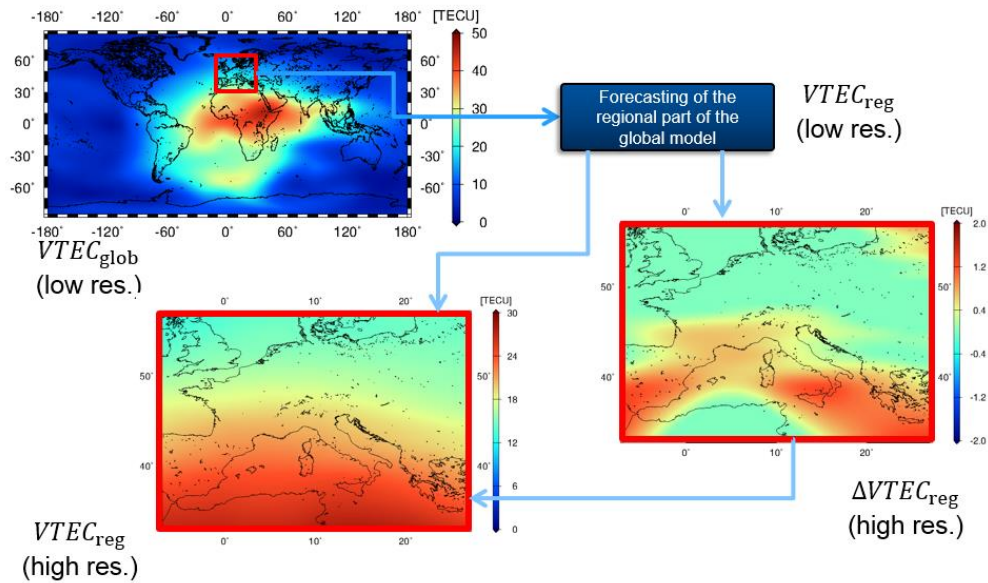


Figure 5.9: Overall procedure to compute the high-resolution regional VTEC maps in real-time. The example follows the strategy introduced in the Figs. 3.6 and 4.1.

5.5 Example of NABS solution in RT

Figure 5.10 shows examples of snapshot maps for a test period covering the April 2nd, 2017. The three rows in the figure present solutions derived at different times, namely, at 10:00, 12:00 and 14:00 UTC. In the first column the VTEC maps derived from the forecast model are depicted. The second column represents the $\Delta VTEC_{reg}$ maps derived from the estimated NABS series coefficients. The last column shows the total VTEC signal which is computed by summing up the forecast model results with the estimated values $\widehat{\Delta VTEC}$ according to Eq. (3.23). The validation of the computed regional VTEC maps in RT for the test period will be performed in the next section.

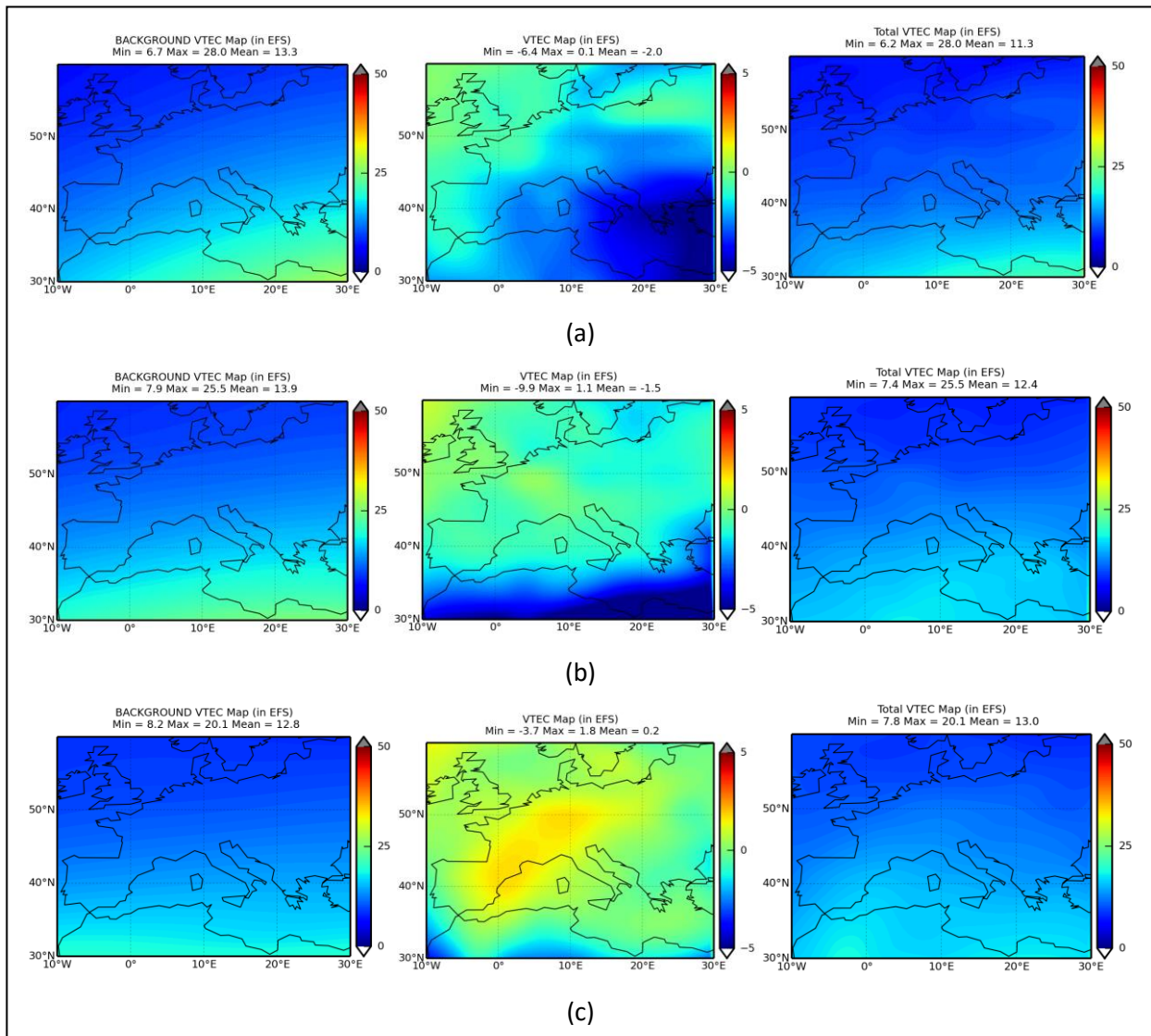


Figure 5.10: Exemplified VTEC solutions calculated according to the RT concept shown in Fig. 5.9 during ionospheric active times for Europe at 10:00 UTC (a), 12:00 UTC (b) and 14:00 UTC (c). The left column shows the VTEC maps derived from the forecast model using Eq. (3.21). The mid column represents the estimated $\Delta VTEC$ solutions according to Eq. (3.18) and the right column composes the total VTEC maps.

6. Validation and verification of ionospheric model results

Introduction

To assess the quality of the VTEC products computed by the described approach, a validation method using the carrier phase observations has been performed. Additionally, a method based on the Jason-2 altimetry VTEC observations was carried out. However, the number of altimetry tracks passing through the area of investigation is very small for a reliable evaluation. Therefore, the validation of the VTEC solutions with altimetry observations has not been considered within AUDITOR.

As assessment criterion, we use statistical values, namely the mean value of the residuals and the standard deviation to evaluate variations of the VTEC products with respect to the reference values derived from the self-consistency analysis (SCA), i.e. the so-called dSTEC analysis. In the following, different ionospheric products provided by the IAACs are considered.

6.1 Self-consistency analysis (dSTEC analysis)

The self-consistency analysis is based on the comparison of STEC values computed from GPS measurements $L_{r,I}^s$ derived from the geometry-free linear combination of carrier-phase according to Eq. (2.2) along a continuous arc and the corresponding STEC values computed from the estimated VTEC maps. Several research groups have provided GNSS-based solutions regarding the STEC modelling with appropriate approaches for quality assessment; see e.g. Orus et al., (2007), Rovira-Garcia et al., (2015), Li et al., (2015) or Brunini et al., (2011).

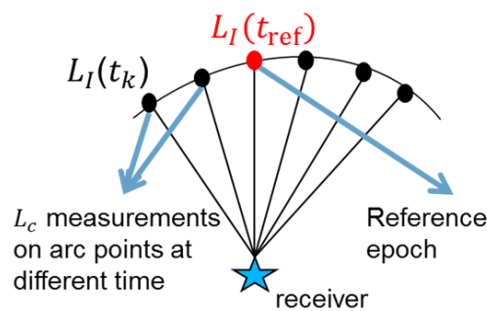


Figure 6.1: Analysis of the $dSTEC_{obs,k}$ values from a continuous arc by subtracting a reference observation.

To be more specific, the group of observations sharing one common ambiguity bias value refers to one arc. On the one hand, differential STEC values, namely $dSTEC_{obs,k}$ can be obtained from the $L_{r,I}^s(t_k) =: L_I(t_k)$ measurements at an observation epoch t_k of one specific arc (see Fig. 6.1) and on the other hand $dSTEC_{map,k}$ derived from the estimated VTEC maps by multiplying the VTEC values with the corresponding mapping function $m(z)$ defined in Eq. (1.5). The resulting test value $dSTEC_k$ for assessing the quality of the products with an accuracy of 0.1 TECU can then be obtained by

$$dSTEC_k = dSTEC_{obs,k} - dSTEC_{map,k}, \quad (6.1)$$

see e.g. Orus et al., (2007) and Feltens et al., (2011).

6.2 Validation results

In the analysis, the VTEC products used for the validation are labelled again as 'codg', 'jplg', 'esag' and 'upcg', which are provided by the individual IAACs, namely CODE, JPL, ESA and UPC. In this sense, the labels 'regNABSrt' and 'regUBSrt' refer to the estimated VTEC maps of our RT solution using the NABS and the UBS approach, respectively. Furthermore, the solution based on the forecast model is labelled as 'fcUBS'.

The geographical locations and the identifiers of the receiver stations selected for the evaluation are shown in Fig 6.2. The receivers are chosen within Europe, i.e. the densification area. As an exemplified analysis, the mean and the standard deviation of the dSTEC variations are computed using the data from the selected stations. The test receivers are chosen carefully around the target area to reveal the VTEC model accuracy characterized by varying the VTEC activity.



Figure 6.2: European receiver stations used for the dSTEC analysis within the AUDITOR project.

The mean values and the standard deviations of hourly dSTEC variations computed from the data of the observation site `YEBE` are presented in Fig. 6.3. The numbers written in parentheses in the legend show the average values of the corresponding statistical measures for the entire day. At the `YEBE` station, the average mean deviations of our RT solutions are 0.09 and 0.12 TECU for the NABS and UBS approaches, respectively, and the average standard deviations for the entire day are 0.36 and 0.34 TECU which are in close agreement with the average standard deviations of the analysis centres ranging from 0.35 to 0.48 TECU. The average standard deviation of the forecast model results reaches to 0.67 TECU and shows high variations during the day compared to the estimated products as it is expected that the forecast model is only providing rather smoothed VTEC solutions.

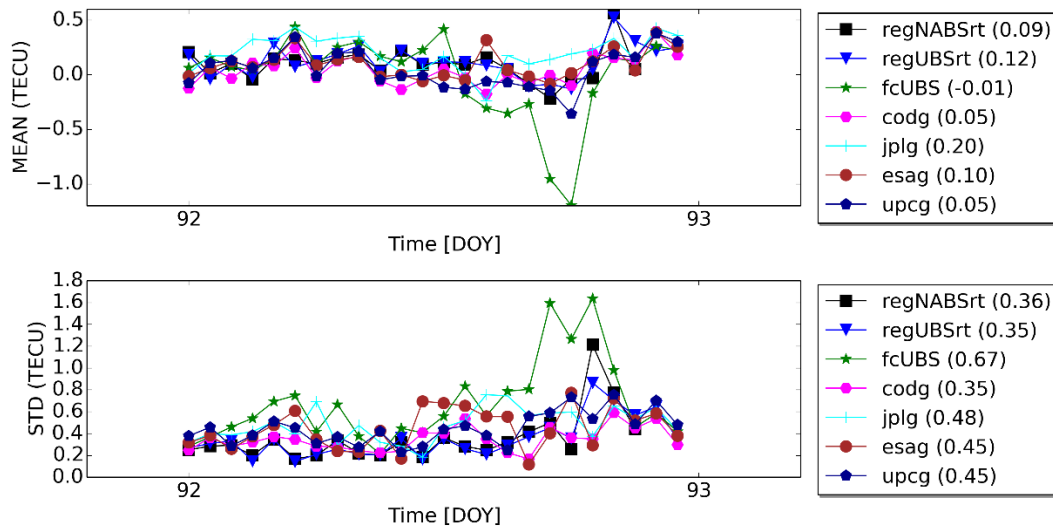


Figure 6.3: Results of the statistical evaluation presenting the differences between the observed and the computed dSTEC values at the station `YEBE` on April 2nd, 2017.

In Fig. 6.4, as a summary of the statistical measures, the average mean values and the average standard deviations are presented for each of the four receiver stations shown in Fig. 6.2 for the entire test period. The dSTEC error for the observation site `NOT1` shows a larger deviation for all VTEC products

in terms of mean value and standard deviation. This might be due to a poor coverage of observations that are acquired from the limited number of receivers located at the Southern EUROPE.

In Fig. 6.4 the values in parentheses in the legend show overall average values computed from all four receivers. The results of our RT solutions in Fig. 6.4 have an overall average bias of 0.02 TECU for the NABS approach and 0.05 TECU for the UBS approach whereas the biases with respect to the other VTEC products vary between -0.02 and 0.15 TECU. The overall average standard deviations range from 0.33 to 0.45 among the solutions of the IAACs; our solutions exhibit 0.42 and 0.43 TECU for the NABS and UBS approaches. The validation analysis reveals that the presented approach is compatible with that of the final products of the analysis centres.

A closer look to Fig. 6.4 reveals that the NABS solution shows smaller biases at the stations `NOT1` and `YEBE` compared to those of the UBS solution. The NABS approach also shows smaller standard deviations at the receiver stations `NOT1` and `BOGI`. At the stations `WTZZ` and `BOGI`, the standard deviations are almost identical for both the NABS and UBS solutions

Moreover, both the NABS and the UBS solutions bring considerable corrections to the results of the forecast model which provides a background solution for the RT approach.

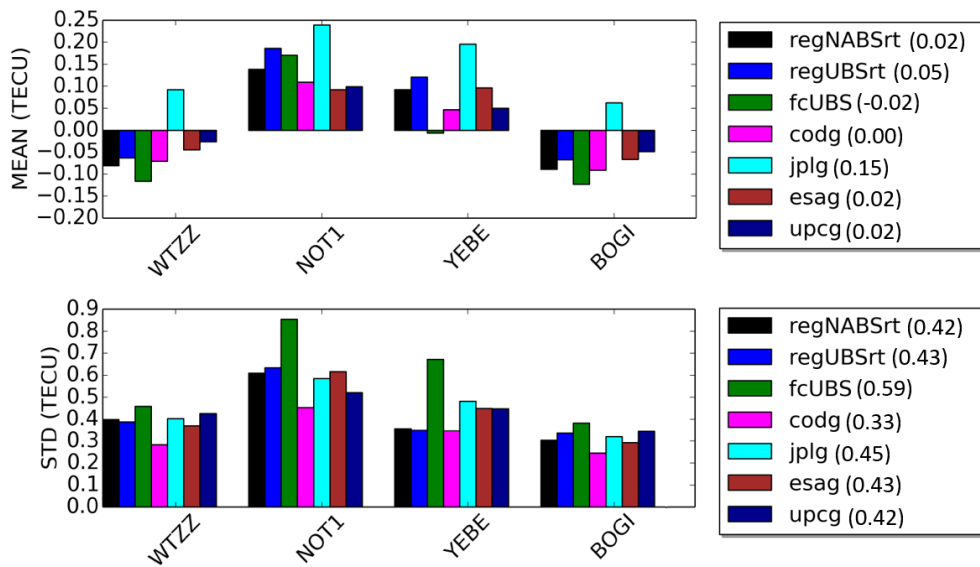


Figure 6.4: Results of the statistical evaluations presenting the differences between the observed and computed dSTEC values

7. Barcelona Ionospheric Mapping (BIM) function

Introduction

Ionospheric delay corrections are significant for precision agriculture users to increase the ambiguity resolution (AR) success rate and reduce the convergence time by means of WARTK. When the distances among the reference stations increase, the AR success rate decreases due to the poor spatial dependence of atmospheric delay. Traditionally, standard mapping function based on the assumption of single layer at one fixed height (Schaer 1999) neglects the variation of ionospheric electron density, which can lead to large mapping errors for the measurements with low elevation; see e.g. Eq. (1.5). If more accurate STEC information could be provided, the AR success rate of WARTK would be improved. Therefore, a new mapping – the Barcelona Ionospheric Mapping (BIM) – function for northern mid-latitudes (BIM-nml) has been proposed, which is more realistic as compared to the traditional approach (1.5) while it is still simple-to-use for GNSS users.

7.1 Two-layer assumption

Assuming the ionosphere is divided vertically into two homogeneous layers, cf. the mid panel of Fig. 1.2. The first ionosphere layer is placed between altitudes of 110 km and 790 km with a central height of 450 km, and the second layer is defined from 790 km to 1470 km altitude with a central height value of 1130 km. We define two ratio values μ_1 and μ_2 as

$$\mu_1 = \frac{N_1}{N_1 + N_2} = \frac{P_1}{P_1 + P_2} = \frac{P_1}{V} \quad (7.1a)$$

$$\mu_2 = \frac{N_2}{N_1 + N_2} = \frac{P_2}{P_1 + P_2} = \frac{P_2}{V} \quad (7.1b)$$

where N_1 and $N_2 = N - N_1$ are the mean electron densities for the corresponding layers. Furthermore, μ_1 and μ_2 can be considered as the shape functions defined for radio occultation inversion (see e.g. Hernández-Pajares et al., 2000) of the bottom side layer and the topside layer only, respectively, i.e. the relative ratio of the mean electron density, N_1 and N_2 , respectively. So, these ratios are also equivalent to the vertical partial electron contents for the first and second layer, as both layers have equal thicknesses. V is VTEC for the entire ionosphere; P_1 and P_2 are the partial vertical electron contents for the first and second layer, respectively.

7.2 BIM modelling based on μ_2

For IPPs which latitudes are between 30° N and 60° N, μ_2 is expressed as the function of t_d and t_h , where t_d means the number of days from the modified Julian day 50965 (this date is DOY 152 of 1998) and t_h means the IPP's local hours. Specifically, μ_2 is modelled as a 4th order polynomial of local hours, and the corresponding time series including the polynomial coefficients are represented as a function of days from the modified Julian day 50965 as

$$\begin{aligned} \mu_2(t_d, t_h) &= a_0(t_d) + a_1(t_d) t_h + a_2(t_d) t_h^2 + a_3(t_d) t_h^3 + a_4(t_d) t_h^4 \\ &= \sum_{i=0}^4 a_i(t_d) t_h^i \end{aligned} \quad (7.2)$$

where t_h is the local hour for the related day of the IPP and t_d is defined as $t_d = \text{mjd} - 50965$. The polynomial coefficients a_i with $i = 0, 1, \dots, 4$ are combined as

$$a_i(t_d) = C_i^{(0)} + \sum_{k=1}^{n_{\tau a_i}} \left(C_i^{(2k-1)} \sin \left(2\pi \frac{t_d}{T_i^{(k)}} \right) + C_i^{(2k)} \cos \left(2\pi \frac{t_d}{T_i^{(k)}} \right) \right) \quad (7.3)$$

where

$C_i^{(0)}$: constant term,

$C_i^{(2k-1)}$: coefficients of sine terms,

$C_i^{(2k)}$: coefficients of cosine terms,

$T_i^{(k)}$: the k th period of the polynomial coefficient a_i ,

$n_{T_{a_i}}$: number of dominant periods of a_i .

With the estimated coefficients it is possible to project STEC to VTEC values by means of the BIM function, i.e.

$$STEC = (1 - \mu_2^{ipp1}) M^{ipp1} V^{ipp1} + \mu_2^{ipp2} M^{ipp2} V^{ipp2} , \quad (7.3)$$

where V^{ipp1} and V^{ipp2} are the VTEC values related to the IPPs IPP1 and IPP2, respectively; see Fig. 7.1. Furthermore, M^{ipp1} and M^{ipp2} are the values of the standard mapping function $m(z)$ from Eq. (1.5), evaluated at the two IPPs IPP1 and IPP2 with the corresponding height values $H_1 = 450$ km and $H_2 = 1130$ km, respectively; see Fig. 7.1.

The values μ_2^{ipp1} and μ_2^{ipp2} are the μ_2 ratio values (7.1b) calculated at IPP1 and IPP2.

7.3 Validation of the BIM-dSTEC assessment

According to the previous research, the GPS ionospheric carrier phase difference $L_{r,I}^S$, for a given satellite-receiver pair, regarding to the value corresponding to the highest elevation ray in the phase-continuous arc of data (see Fig. 6.1), provides a very precise ionospheric truth of the STEC referred to the value at maximum elevation, dSTEC, in space and time (typically more accurate than 0.1 TECU, see for instance Orús et al., 2005, Feltens et al., 2011). It has been used to compare the performances of different ionospheric models in the IGS context (Hernández-Pajares et al., 2016, 2017). In addition, the dSTEC observable (6.1) is very sensitive to changes of the elevation. So it is a good ionospheric reference truth for the assessment of the mapping function.

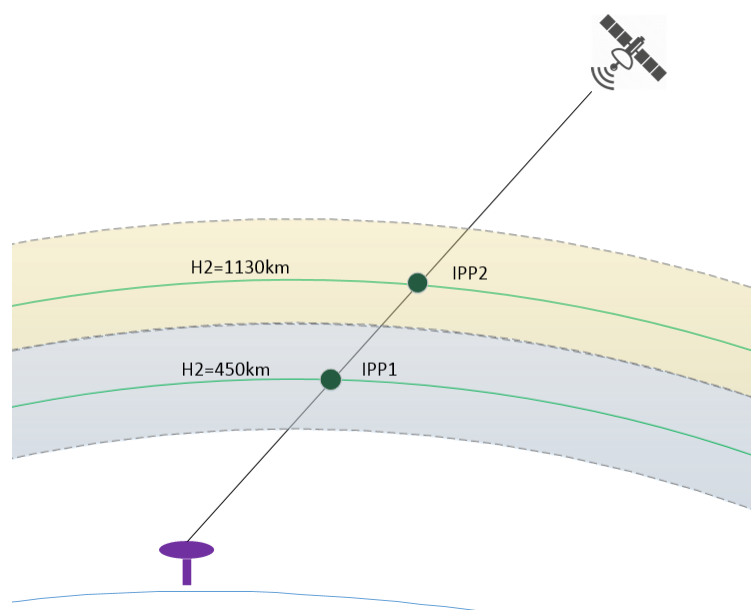


Figure 7.1: The diagram of BIM; IPP1 and IPP2 are the ionospheric pierce points along the ray path at the height values of the two layers.

In order to evaluate the performance of the BIM, the dSTEC data in the whole year 2014 from all available IGS stations which are not used for the generation of UQRG¹ GIMs in the study region has been selected. There are 14 available stations in the range between 30° N and 60° N where, however, only 8 of them – marked in black in Figure 7.2 – have enough data for statistical investigations.

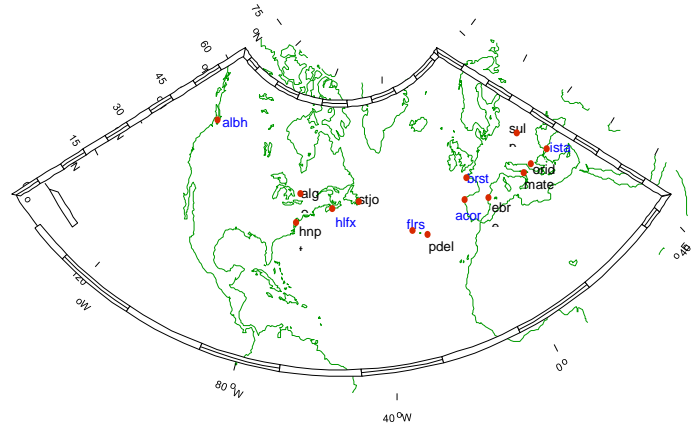


Figure 7.2: IGS stations which are not used for the generation of the UQRG GIM in 2014 for external assessment of the BIM performance. The stations in blue were not used for statistical investigations due to very limited data for only a few available days.

By taking the station orid as an example, it is obvious that the RMS value of the dSTEC residual error with the BIM (7.3) is smaller than that computed with the standard mapping function (1.5), particularly for the signals with low elevations. Specifically, from DOY 16 to DOY 30, the RMS of dSTEC has been reduced by approximately 0.5 to nearly 1.0 TECU. The results for the 234-day analysis in 2014 indicate that the BIM performs better than the standard mapping function over 210 days (more than 90%) in terms of RMS. As for 8 IGS stations statistical investigations can be performed, the BIM performs well for 6 stations, except the stations `algo` and `stjo`, which might be affected by the high magnetic latitude. The number of days where the dSTEC RMS values are decreased accounts for more than 70% of the available days in 2014. Meanwhile, the CODG GIM and the JPLG GIM are also used for assessment. As shown before the BIM improves dSTEC using JPLG GIM as well dominantly for all the 14 available stations, reinforcing the physical consistency of the BIM, regardless of the UPC-TOMION model used originally to compute it.

As already mentioned at the end of Subsection 2.4 the BIM function is applied in our procedure as shown in the Figs. 3.6 and 4.1 for projecting the estimation \widehat{VTEC}_{reg} computed at the IPPs IPP1 and IPP2 (see Fig. 7.1) via the relation

$$STEC = (1 - \mu_2^{ipp1}) M^{ipp1} \widehat{VTEC}_{reg}^{ipp1} + \mu_2^{ipp2} M^{ipp2} \widehat{VTEC}_{reg}^{ipp2} \quad (7.4)$$

into the STEC value between the satellite and the receiver. This value will be used to correct the ionospheric delay and to reduce the convergence time in precision agriculture. However, we have to state that at the border lines of the region of investigation, i.e. the densification area we have to distinguish between the high-resolution VTEC values \widehat{VTEC}_{reg} within the area and the low-resolution VTEC values \widehat{VTEC}_{glob} outside the area. These circumstances can be seen in Fig. 5.9.

¹ The UQRG-labelled Global Ionospheric Maps correspond to UPC-IonSAT 15-minute resolution GIMs at 5°/2.5° resolution in longitude/latitude. These GIMs are generated with a 1-day latency and, for their computation, the 2-layer voxel tomographic model is used as well as the Kriging interpolation technique; see Hernández-Pajares et al. (2017)

8. Conclusions

In this deliverable we presented a procedure to calculate high-precision and high-resolution VTEC maps from NRT and RT GNSS observations based on B-spline series expansions as an alternative of the traditional VTEC modelling approach based on spherical harmonics. The basic steps of the procedure are explained in detail in this report and visualized within the two flowcharts shown in the Figs. 3.6 and 4.1. Basically the procedure consists of a global low-frequency part and a high-resolution model part applied to areas of interest, such as regions used for precision farming. As study area we used in this deliverable an area covering the largest part of Europe. It has to be stated that this choice became necessary since our global model reflects a spectral range up to a resolution level which corresponds to a degree of around 15 in case of a spherical harmonic representation. If our global model covers a spectral range, e.g., until degree 20 or 30, the regional area of investigations could become much smaller. As indicated in the Subsection 3.3 by means of the Eqs. (3.15) and (3.16) the highest resolution level of our global approach depends on the distribution of the input data, i.e. the average values of the sampling intervals between the geographical locations of the IPPs related to the GNSS measurements; see Fig. 3.4.

Kalman filter procedures are used to estimate the unknown parameters for both the global model and the regional densification model part. A forecasting became necessary to bridge the gap between the NRT global GNSS input data and the regional RT input data. The estimation procedures also allow the computation of all error or standard deviation maps related to the VTEC products.

To use the estimated VTEC information, e.g. in precision agriculture, it must be transferred to the user. It was already stated in the deliverable D4.1 of the AUDITOR project that there are basically two options for setting up a message based on our B-spline modelling approach, namely providing

- (1) VTEC B-spline series coefficients or
- (2) VTEC grid values.

As discussed in the Introduction we recommend the second option, since in this case no encoding procedure is necessary for computing the regional VTEC values from B-spline series coefficients. This procedure is especially in case of the NABS functions not an easy task. In case of option (2) just a simple interpolation procedure has to be applied to compute the high-precision VTEC value at any arbitrary geographical location at any specific time.

For the application of the developed approach the creation and implementation of an appropriate message based on the VTEC grid values is necessary. This way, the information could be provided via the iBOGART cloud server to the receiver, i.e. to the user.

However, the development of such a message was not part of WP 4 within the AUDITOR project.

9. References

AUDITOR D1.1: State of the Art

AUDITOR D4.1: IBOGART design, implementation and validation

- Birch M.J., Hargreaves J.K., and Bailey G. J. (2002): On the use of an effective ionospheric height in electron content measurement by GPS reception. *Radio Science*, Vol. 37, No. 1, 1015, doi: 10.1029/2000RS002601.
- Brunini C., Camilion E., and Azpilicueta F.: Simulation study of the influence of the ionospheric layer height in the thin layer ionospheric model, *Journal of Geodesy*, 85, 637- 645, doi: 10.1007/s00190-077-0470-2, 2011.
- Chen P., Yao Y., and Yao W.: Global ionosphere maps based on GNSS, satellite altimetry, radio occultation and DORIS, *GPS Solutions*, 1-12, doi: 10.1007/s10291-016-0554-9, 2016.
- Ciraolo L., Azpilicueta F., Brunini C., Meza A., and Radicella S. M.: Calibration errors on experimental slant total electron content (TEC) determined with GPS, *Journal of Geodesy*, 81, 111-120, doi: 10.1007/s00190-006-0093-1, 2007.
- Dach R.: Center for Orbit Determination in Europe (CODE). IGS Technical Report 2012, 35-46, Jet Propulsion Laboratory, 2012.
- Dach R., Hugentobler U., Fridez P., and Meindl M.: Bernese GPS Software, Version 5.0. Astronomical Institute, University of Bern, 2007.
- Dettmering D., Schmidt M., Heinkelmann R., and Seitz M.: Combination of different space-geodetic observations, for regional ionosphere modeling, *Journal of Geodesy*, 85, 989-998, doi: 10.1007/s00190-010-0423-1, 2011.
- Erdogan E., Schmidt M., Seitz F., Durmaz M.: Near real-time estimation of ionosphere vertical total electron content from GNSS satellites using B-splines in a Kalman filter, *Annales Geophysicae*, 35, 263-277, doi: 10.5194/angeo-35-263-2017, 2017.
- Feltens J., Angling M., Jackson-Booth N., Jakowski N., Hoque M., Hernández-Pajares M., Aragón-Ángel A., Orús R., and Zandbergen R.: Comparative testing of four ionospheric models driven with GPS measurements, *Radio Science*, 46, doi: 10.1029/210RS004584, 2011.
- Fu L.-L., and Cazenave A. (Eds.): *Satellite Altimetry and Earth Sciences A Handbook of Techniques and Applications*, Academic Press Inc., San Diego, California, 2001.
- Gelb A. (Ed.): *Applied Optimal Estimation*, MIT Press, Cambridge, 1974.
- Grewal M. S. and Andrews, A. P.: *Kalman Filtering: Theory and Practice Using MATLAB*, John Wiley & Sons, Inc., 3rd Edn., Hoboken, New Jersey, 2008
- Hagood M. A.: *Space Physics Coordinate Transformations: A User Guide*, *Planetary and Space Science*, 40(5), 711-717, 1992.
- Hernández-Pajares M., Juan J.M. and Sanz J.: New approaches in global ionospheric determination using ground GPS data. *J. Atmos. Sol. Terr. Phys.*, 61(1999), 1237–1247.3, 66, 1999.
- Hernández-Pajares M, Juan J M, Sanz J.: Improving the Abel inversion by adding ground GPS data to LEO radio occultations in ionospheric sounding. *J. Geophysical Research Letters*, 2000, 27(16), 2473-2476.
- Hernández-Pajares M., Juan J., Sanz J., and Garcia-Fernandez M.: Towards a more realistic ionospheric mapping function. In XXVIII URSI General Assembly, Delhi, 2005.
- Hernández-Pajares, M., Roma-Dollase, D., Krankowski, A., Ghoddousi-Fard, R., Yuan, Y., Li, Z., Zhang, H., Shi, C., Feltens, J., Komjathy, A., Vergados, P., Schaer, S., Garcia-Rigo, A., and Gómez-Cama, J. M.: Comparing performances of seven different global VTEC ionospheric models in the IGS Context,

- in: IGS Workshop, 8–12 February 2016, Sydney, Australia, International GNSS Service (IGS), 1–31, 2016.
- Hernández-Pajares M., Roma-Dollase D., Krankowski A., García-Rigo A., and Orús-Pérez R.: Methodology and consistency of slant and vertical assessments for ionospheric electron content models. *J Geod.* doi:[10.1007/s00190-017-1032-z](https://doi.org/10.1007/s00190-017-1032-z), 2017
- Huang Z. and Yuan H.: Analysis and improvement of ionospheric thin shell model used in SBAS for China region. *Advances in Space Research*, 51(11):2035–2042, 2013.
- Hugentobler U. et al.: CODE IGS Analysis Center Technical Report 2003/2004. IGS 2003-2004 Technical Reports, IGS, Central Bureau, 2008.
- Juan J.M., Rius A., Hernández-Pajares M. and Sanz J.: A two-layer model of the ionosphere using Global Positioning System data. *Geophys. Res. Lett.*, 24(4), 393–396. 3,66, 1997
- Kalman R.: A new approach to linear filtering and prediction problems, *Journal of Basic Engineering*, 82, 35-45, 1960.
- Koch, K.-R.: Parameter estimation and hypothesis testing in linear models. Springer, Berlin, ISBN 3-540-65257-4, 1999.
- Komjathy A. and Langley R. B.: The effect of shell height on high precision ionospheric modeling using GPS. In *International GPS Service for Geodynamics (IGS) Workshop*, number March, pages 19–21, Silver Spring, 1996.
- Kuklinski W.S.: Ionospheric tomography via iterative cross-entropy minimization. *Radio Sci.*, 32(3), 1037–1049. 3, 66, 1997.
- Laundal K. M., Richmond A. D.: Magnetic Coordinate Systems, *Space Science Reviews*, 206, 27-59, doi: [10.1007/s112140-016-0275-y](https://doi.org/10.1007/s112140-016-0275-y), 2017.
- Leitinger R., Nava B. and Hochegger S., G. and Radicella S.: Ionospheric profilers using data grids. *Phys Chem Earth*, 26(5), 293–301, 2001.
- Li Z., Yuan Y., Wang N., Hernandez-Pajares M., and Huo X.: SHPTS: Towards a new method for generating precise global ionospheric TEC map based on spherical harmonic and generalized trigonometric series functions, *Journal of Geodesy*, 89, 331-345, doi: [10.1007/s00190-014-0778-9](https://doi.org/10.1007/s00190-014-0778-9), 2015.
- Limberger, M.: Ionosphere modeling from GPS radio occultations and complementary data based on B-splines, PhD thesis, Technical University Munich, 2015.
- Liu, Z.Z. and Gao, Y.: Development and Evaluation of a New 3-D Ionospheric Modeling Method. *Navigation*, 51(4), 311–329, 2004.
- Liu L., Wan W., and Ning B.: A study of the ionogram derived effective scale height around the ionospheric hmF2. *Ann. Geophys.*, 24, 851–860. 66, 71, 114, 2006
- Lyche T. and Schumaker L. L.: A Multiresolution Tensor Spline Method for Fitting Functions on the Sphere, *SIAM Journal on scientific Computing*, 22(2), 724-746, doi: [10.1137/S1064827598344388](https://doi.org/10.1137/S1064827598344388), 2000.
- Mannucci A. J., Wilson B. D., Yuan D. N., Ho C. H., Lindqwister U.J., and Runge T.F.: A global mapping technique for GPS-derived ionospheric total electron content measurements, *Radio Science*, 33, 565-582, doi: [10.1029/97RS02707](https://doi.org/10.1029/97RS02707), 1998.
- Orús R., Hernández-Pajares M., Juan J. M., et al.: Improvement of global ionospheric VTEC maps by using kriging interpolation technique. *Journal of Atmospheric and Solar-Terrestrial Physics*, 2005, 67(16), 1598-1609.
- Orus R., Cander L. R., and Hernandez-Pajares M.: Testing regional vertical total electron content maps over Europe during the 17-21 January 2005 sudden space weather event, *Radio Science*, 42, RS3004, doi: [10.1029/2006RS003515](https://doi.org/10.1029/2006RS003515), 2007.

- Panzetta F., Bloßfeld M., Erdogan E., Schmidt M., Müller H.: Absolute thermospheric density estimation from SLR observations of LEO satellites - A case study with ANDE-Pollux satellite. *J Geodesy* (in review), 2017.
- Rama Rao P. V. S., Niranjana K., Prasad D. S. V. V. D., Gopi Krishna S., and Uma G.: On the validity of the ionospheric pierce point (IPP) altitude of 350 km in the Indian equatorial and low-latitude sector. *Annales Geophysicae*, 24(8):2159–2168, 2006.
- Rovira-Garcia A., Juan J. M., Sanz J., and Gonzalez-Casado G.: A Worldwide Ionospheric Model for Fast Precise Point Positioning, *IEEE T. Geoscience Remote Sensing*, 53, 4596-4604, doi: 10.1109/TGRS.2015.2402598, 2015.
- Schaer S.: Mapping and predicting the Earth's Ionosphere Using the Global Positioning System, PhD thesis, University of Bern, Bern, 1999.
- Simon D.: Optimal State Estimation, John Wiley & Sons, Inc., Hoboken, New Jersey, doi: 10.1088/1741-2560/2/3S07, 2006
- Schmidt M.: Wavelet modelling in support of IRI, *Advances in Space Research.*, 39, 932-940, doi: 10.1016/j.asr.2006.09.030, 2007.
- Schmidt M., Bilitza D., Shum C.K., and Zeilhofer C.: Regional 4-D modeling of the ionospheric electron density, *Advances in Space Research*, 42, 782-790, doi: 10.1016/j.asr.2007.02.050, 2008.
- Schmidt M., Dettmering D., and Seitz F.: Using B-Spline Expansions for Ionosphere Modeling, in: *Handbook of Geomathematics*, edited by: Freeden, W., Nashed, M. Z., and Sonar, T., 939-983, doi: 10.1007/978-3-642-54551-1_80, Springer Berlin Heidelberg, Berlin, Heidelberg, 2015.
- Schumaker L. L. and Traas C.: Fitting scattered data on spherelike surfaces using tensor products of trigonometric and polynomial splines, *Numerische Mathematik.*, 60, 133-144, doi: 10.1007/BF01385718, 1991.
- Smith D. A., Araujo-Pradere E. A., Minter C., and Fuller-Rowell T.: A comprehensive evaluation of the errors inherent in the use of a two-dimensional shell for modeling the ionosphere. *Radio Science*, 43(6):RS6008, 2008.
- Tseng K.-H., Shum C. K., Yi Y., Dai C., Lee H., Bilitza D., Komjathy A., Kuo C. Y., Ping J., and Schmidt M.: Regional Validation of Jason-2 Dual-Frequency Ionosphere Delays, *Marine Geodesy*, 33, 272-284, doi: 10.1080/01490419.2010.487801, 2010.
- Zeilhofer C.: Multi-dimensional B-spline Modeling of Spatio-temporal Ionospheric Signals. Master's thesis, DGK Reihe A 123, Deutsche Geodätische Kommission, München, 2008.
- Zeilhofer C., Schmidt M., Bilitza D., and Shum C.K.: Regional 4-D modeling of the ionospheric electron density from satellite data and IRI. *Adv. Space Res.*, 43(11), 1669–1675, 2009.